Optimization of Gabor Lenses for In Vitro Experiments with Laser-Accelerated Ion Beams

Master's Thesis in Physics

Presented by

Moritz Sebald

23.10.2018

Friedrich-Alexander-Universität Erlangen-Nürnberg

Supervisors:
Prof. Dr. Hommelhoff
Prof. Dr. Bert

Carried out at Imperial College London

Abstract

In future, novel treatment devices based on laser-plasma acceleration could offer a compact and cost-saving alternative for the synchrotron accelerators currently used in ion beam therapy. In a first step towards the therapeutic application of laser-accelerated ions their physical and radiobiological behaviour has to be investigated in in vitro experiments and compared to conventionally accelerated ion beams. Due to the short pulse duration, large energy spread and angular divergence of laser-accelerated ion beams Gabor plasma lenses could offer favourable properties for their beam transport.

This work mainly investigated the unexpected conversion of a proton pencil beam into rings by Imperial College London's Gabor lens prototype. The conversion can be explained by the formation and rotation of an electron bulk in the non-neutral plasma (NNP) of the lens. To investigate the non-neutral electron plasma confined within the lens two experiments were designed and tested: A radio frequency (RF) emission measurement for the detection of possible RF-signals emitted by the rotating electron bulk and a RF-transmission measurement for obtaining information about the NNP's density. It was shown that RF-antennas are capable of transmitting signals in the frequency range of 20 MHz to 200 MHz through an Gabor lens without NNP. RF-emission measurements on stable and unstable plasma states demonstrated that the antennas are capable of detecting RF-signals emitted by unstable plasma states. In the case of the stable plasma state, which is used for ion focussing and beam transport, no RF-signal was detected. This indicates that the electron bulk is not merely rotating but following a helical trajectory.

The data collected are a first step to understand the formation of rings. In parallel investigations on vacuum leaks detected during a connection to the Cerberus laser system were started. Identifying the cause of the conversion and closing the vacuum leaks are important steps towards the application of the Gabor lens prototype in in vitro experiments.

Acknowledgements

Hereby, I would like to thank my principal supervisor Dr. Jürgen Pozimski for his time to share his knowledge, his supervision and ideas and Prof. Kenneth Long for his support during my stay at Imperial College London. I also wish to thank my two supervisors Prof. Christoph Bert and Prof. Peter Hommelhoff at Friedrich-Alexander-Universität Erlangen-Nürnberg for their input and encouragement. Furthermore, I wish to thank the mechanical and electrical workshop of the High Energy Physics Group at Imperial College London for their advice and input. To finish, I would like to thank my family and friends for their encouragement, prudent advice and time for proof-reading.

Contents

List of Figures

List of Tables

Chapter 1

Introduction

According to the International Agency for Research in Cancer (IARC) "cancer is expected to rank as the leading cause of death and the single most important barrier to increasing life expectancy in every country of the world in the 21st century" (Bray et al. 2018). Cancer treatment is conducted in a multidisciplinary approach comprising radiation therapy (RT), surgery, chemotherapy, immunotherapy and hormonal therapy. Approximately 50 % of all cancer patients receive RT during their course of illness, making it an important component of cancer treatment (Baskar et al. 2012). The main goal of RT is to deliver a lethal dose to the tumour while sparring healthy tissue to a maximum extent. Generally, patients are treated with x-rays but since Wilson (1946) proposed the therapeutical application of high-energetic protons and heavier ions, ion beam therapy gained considerable importance. The main advantage of ion beams in RT is their favourable depth-dose profile for treatment of deep-seated local tumours, see figure 1.1. Ions heavier than protons addi-

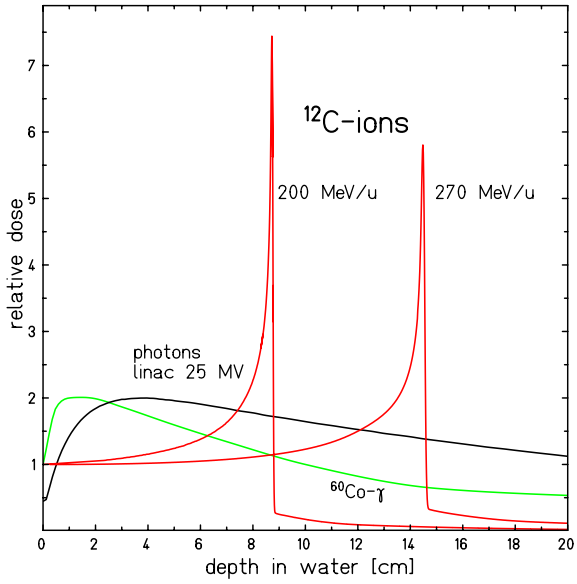

Figure 1.1: Comparison of Depth-Dose Profiles of Co-60 γ Radiation, MV Photons, and C-12 Ions in Water (Schardt et al. 2010)

tionally exhibit an increased relative biological effectiveness (RBE) compared to x-rays and protons (Tobias & Todd 1967; Chen et al. 1981). Besides investigating the physical and biological advantages of ion beams dedicated research centres around the world developed technical solutions for patient treatment (Chu et al. 1993; Pedroni et al. 1995; Haberer et al. 1993). Subsequent clinical trials proved the clinical effectiveness and technical feasibility of ion beam therapy as well as the superior performance for a number of tumour entities (Durante & Loeffler 2010; Debus et al. 2000). Nowadays, 76 centres worldwide provide ion beam therapy with protons and or carbon ions (PTCOG 2018) but the widespread introduction of ion beam therapy is inhibited by the high costs of accelerator, beam delivery system and maintenance (Pozimski et al. 2013).

Simultaneously to the developments in ion beam therapy based on cyclotron and synchrotron

acceleration, the laser-plasma acceleration of ions has made tremendous progress. Hence, the therapeutic use of laser-plasma accelerated ions was proposed (Bulanov & Khoroshkov 2002; Schwoerer et al. 2006; Bulanov et al. 2014) with the goal of building compact and cost-saving medical treatment devices. The physical properties of laser-accelerated ion beams such as short pulse duration, large energy spread and angular divergence make the capture, focusing and beam transport of such beams a challenging task (Pozimski & Aslaninejad 2013). Furthermore, before starting any medical application also the RBE of laser-accelerated ions has to be determined and compared to the RBE of conventionally accelerated ions (Kraft et al. 2010).

Encouraging results from theoretical and numerical investigations showed that a Gabor (space charge) lens lattice is suitable for capturing, focussing and the transport of laser-accelerated ion beams (Pozimski et al. 2016). Thus, a Gabor-lens prototype was build at Imperial College London (United Kingdom) and a potential beamline for a laser-driven hadron in vivo irradiation facility has been designed, see figure 1.2. The proposed beamline consists of four Gabor lenses for beam capture, focusing, transport and dose selection, two cavities for reducing the momentum spread, an aperture for energy selection, a dipole for a 90 degree deflection of the ion beam and a radiobiological end-station for in vivo experiments and dose diagnostics. During the first beam test of

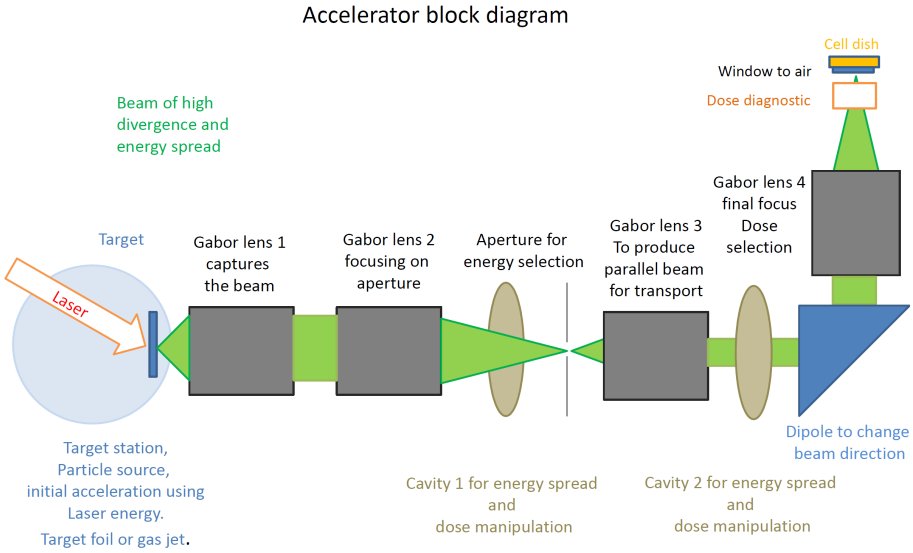

Figure 1.2: Accelerator Block Diagram for a laser-driven Hadron in vivo Irradiation Facility based on a Gabor Lens Lattice for Ion Capture, Focussing and Transport (Pozimski 2017)

the Gabor lens prototype it unexpectedly converted the incoming 1 MeV pencil proton beam into rings (Posocco et al. 2016). Hence, the two main purposes of this work are

1. investigating the unexpected conversion of the pencil proton beam into rings by the Gabor lens prototype and
2. specifying the necessary energies of different ions for the use in in vivo experiments.

Chapter 2

Material and Methods

2.1 Simulations on the Penetration Depth of Ions Through Matter

For the design of a particle in vitro irradiation facility based on laser acceleration a profound understanding of the energy losses of different ions in the radiobiological end-station is necessary since these losses determine the requirements for the beamline and the laser system. It is also the basis for improvements of the materials and devices build into the end-station. For this purpose SRIM (Stopping and Range of Ions in Matter) was used to investigate the energy losses of ions in the end-station as proposed by Kraft et al. (2010). SRIM combines a large database of materials and compounds with experimentally determined stopping powers for ions with a Monte Carlo simulation, which is called TRIM (Transport of Ions in Matter). TRIM calculates the interactions of energetic ions with amorphous targets. For this purpose it makes several physical approximations in the calculations (Ziegler et al. 2008, p. 7-3) and the two most important ones are:

- using an analytic formula for determining atom-atom collisions and
- using the concept of Free-Flight-Path between collisions.

The proposed radiobiological end-station is called iDocis and is an integrated dosimetry and cell irradiation system. The setup is shown in figure 2.1. It consists of a kapton window, which isolates the iDocis from the vacuum system of the beamline, an ionization chamber (IC) for online dosimetry and an irradiation site with variable insets. The cell sample is used for radiobiological experiments whereas the Farady cup is used for absolute dosimetry and the radiochromic films (RCF) stack for the measurement of the 2D dose and spectral energy distribution. For radiobiological experiments the setup consists of the kapton window, the IC and the cell sample. The parameters of the individual components are listed in table 2.1. As not all materials that were used in the iDocis

Table 2.1: iDocis Components and Parameters

Component	Parameters
Kapton Window	25 μm of kapton and 35 mm in diameter (Richter et al. 2011)
IC	Three metallized kapton foils each 7.5 μm with a gap size of 6.6 mm
Cell sample	Squamous cell carcinoma (SCC) on biofilm (lumox®, 50 μm) at bottom of 4-well slide closed with sterile Parafilm®

are part of the SRIM database similar materials were chosen for the simulations. A list of the components and the settings used during the simulations can be found in table 2.2. Figure 2.2 illustrates the design of the setup used for the simulations. The gap between kapton window and IC as well as the gap between IC and irradiation side was assumed to be 500 μm each even though the article does not give any distance for the gaps. The 4-well slide (Sarstedt AG and Co., Nümbrecht, Germany) consists of a slide with a 50 μm lumox® film and a frame made out of polystyrene. As

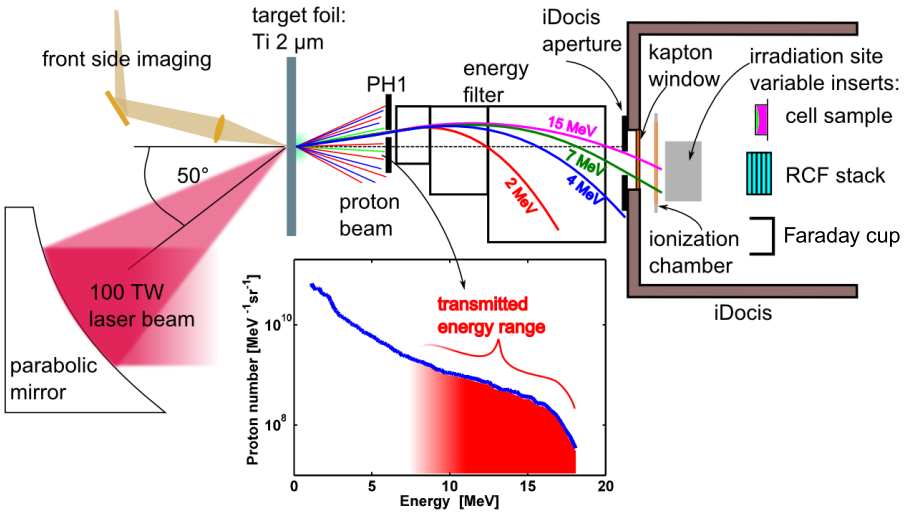

Figure 2.1: Experimental Setup Designed by Kraft et al. (2010)

the material and thickness of the slide is not specified by the company a 100 μm slide has been assumed. Furthermore, instead of lumox® polyethylene was used as film, the skin cancer cells SCC were replaced by skin cells of type 1 and the parafilm ® by polyethylene. The average diameter of a human skin cells is 30 μm (Learn.Genetics 2018) and the average thickness of parafilm® is 0.13 mm (SIGMA 2010). For precise absolute dosimetry it is necessary that protons are not fully

Table 2.2: Components and Parameters Used for Simulations

Component	Parameters
Kapton Window	25 μm of kapton polyimide film
IC	Three kapton polyimide films each 7.5 μm with a gap size of 6.6 mm of dry air
Air	500 μm of dry air on left and right side of IC
Cell Sample	100 μm of polystyrene, 50 μm of polyethylene, 30 μm of skin cells type 1 and 0.13 mm of polyethylene

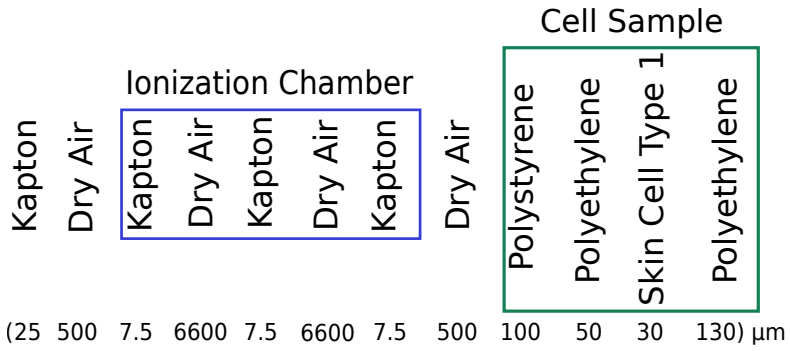

Figure 2.2: Schematic Overview of the Materials and their Dimensions Used in the SRIM Simulations

stopped in the cell monolayer (Kraft et al. 2010). Therefore, the energy of the protons was set to a value at which all protons pass the boundary between skin cell type 1 monolayer and the polyethylene layer that closes the well. In the simulations the boundary lies at 14.43 mm. Besides hydrogen ions also helium, lithium and carbon ions were used for the simulations. The number of particles was set to 10,000 in all of the SRIM simulations.

For the design of a beamline with a 90 degree bend of the ion beam further simulations on the penetration depth of ions of different magnetic rigidity in water were conducted. Bending the

ion beam into a vertical orientation improves cell dish handling and reproducibility of in vitro experiments compared to a horizontal beam orientation. Mainly, because a cell monolayer can not be irradiated alone but always requires a certain amount of cell culture medium added into the Petri dish. Thus, in vertical orientation gravity promotes the formation of a homogeneous cell sample whereas in horizontal orientation special measures have to be taken to ensure homogeneity of the cell sample. The magnetic rigidity of a particle is defined as

$$B\rho = \frac{p}{q}, \tag{2.1}$$

with the particles gyradius ρ, relativistic momentum p and charge q and the external magnetic field B. It is a measure of the resistance of a particle to deflection from its trajectory by an external magnetic field. So the lower the magnetic rigidity the stronger the magnetic field has to be to bend the particle beam. In a first step the magnetic rigidity of H-1, He-3, He-4 and C-12 was compared for a penetration depth of 5 cm to estimate how the requirements on the dipole, which deflects the ion beam, alter for the different ions. For ions of identical magnetic rigidity the parameters of the dipole would not have to be changed, making the setup less complex and expensive. Thus the energy and penetration depth of He-4 and C-12 were compared for a given magnetic rigidity.

2.2 The Gabor Lens

In 1947 D. Gabor proposed a magnetron of special design, nowadays known as the Gabor lens, which could be used to focus positive ions (Gabor 1947). His idea was to confine electrons produced by a hot cathode inside the magnetron by a crossed configuration of a radial magnetic field and a longitudinal electric field. The radial magnetic field is produced by two coils of uneven length and the electric field is produced by a cylindrical electrode at high positive potential and a cathode. The initial design of the Gabor lens is illustrated in figure 2.3 . Under the assumption that an equilibrium is established inside the lens and uniformity of the electron cloud he calculated the space charge density $\rho_{H,G}$ and the radial electric field $\mathrm{E}_{r,G}$ produced by the space charge in Gaussian units.

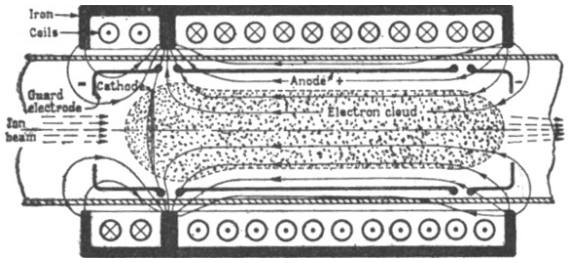

Figure 2.3: Initial design of Gabor's Magnetron Lens (Gabor 1947)

$$\rho_{\mathrm{H,G}} = -\frac{e_{\mathrm{G}} H_{\mathrm{G}}^2}{8\pi m_{\mathrm{e}} c_{\mathrm{G}}^2} \tag{2.2}$$

$$E_{\mathrm{r,G}} = -\frac{e_{\mathrm{G}} H_{\mathrm{G}}^2}{4 m_{\mathrm{e}} c_{\mathrm{G}}^2} r \tag{2.3}$$

Using the conversion factors between Gaussian and SI units listed in table 2.3 and the relation $\vec{B} = \mu_0 \vec{H}$ for vanishing magnetization $\vec{M}$ equations (2.2) and (2.3) are obtained in SI units.

$$\rho_{\mathrm{H,SI}} = -\frac{e_{\mathrm{SI}} \epsilon_0 B_{\mathrm{SI}}^2}{2 m_{\mathrm{e}}} \tag{2.4}$$

$$E_{\mathrm{r,SI}} = -\frac{e_{\mathrm{SI}} B_{\mathrm{SI}}^2}{4 m_{\mathrm{e}}} r \tag{2.5}$$

The radial electric field E_{r} shows the linear dependency on the radius which is required for a focusing lens.

Table 2.3: Conversion Table

Gaussian Units	SI Units
ρ_{G}	$\rho_{\mathrm{G}} = \frac{\rho_{\mathrm{SI}}}{\sqrt{4\pi\epsilon_0}}$
H_{G}	$H_{\mathrm{G}} = \sqrt{4\pi\mu_0} H_{\mathrm{SI}}$
e_{G}	$e_{\mathrm{G}} = \frac{e_{\mathrm{SI}}}{\sqrt{4\pi\epsilon_0}}$
c	$c = \frac{1}{\sqrt{\epsilon_0\mu_0}}$

2.2.1 Non-Neutral Plasma Confinement

A non-neutral plasma is defined as a many body collection of particles in which there is no overall charge neutrality (Davidson 2001, p.1). In contrast to quasi-neutral plasmas non-neutral plasmas (NNPs) exhibit intense self-electric fields. Many of the collective properties such as plasma frequency, plasma waves, instabilities and Debye shielding found in quasi-neutral plasmas are also found in NNPs. However, the intense self-fields produced in NNPs can have a large influence on the behaviour and stability of theses plasmas.

In a Gabor lens the crossed configuration of a magnetic and a electric field is used to confine the NNP,which is also referred to as space charge, within the lens. As shown in figure 2.4 a solenoid can be used to produce the axial magnetic field for radial confinement and a electrode system consisting of a cylindrical anode and a pair of ground electrodes for longitudinal confinement. With this configuration the space charge is confined in all directions and the confining fields determine the maximum space charge density in each direction.

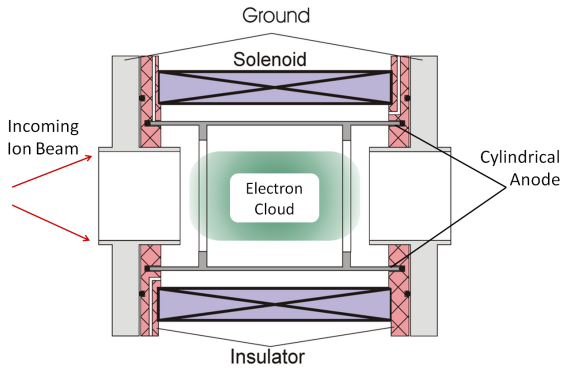

Figure 2.4: Schematic Overview of the Electron Confinement in a Gabor Lens (Hughes 2014, p. 14)

Radial Confinement

For the theoretical treatment of the longitudinal and radial confinement of the non-neutral electron plasma inside the Gabor lens the research so far suggests to consider a pure, non-relativistic, collisionless, cold electron plasma in steady state (Gabor 1947; Pozimski 1990, p.22 & 23; Davidson 2001, p.30; Meusel 2006, p.10). Due to these assumptions the non-neutral electron plasma can be described in the macroscopic fluid description. The electrons inside the lens are radially confined by an axial magnetic field. In steady state the the electrons rotate around the symmetry axis of the lens, such that the inwards facing radial Lorentz force F_{L} is balanced by the outwards facing electrostatic force F_{E} and the centrifugal force F_{C} as illustrated in figure 2.5. The following mathematical description of the radial confinement follows the argumentation of (Davidson 2001, p.39 - 56). The force balance equation is given by

$$-\frac{m_{\mathrm{e}} v_{\mathrm{e},\theta}^2}{r} = -eE_{\mathrm{r}} - ev_{\mathrm{e},\theta} B_{\mathrm{z}}, \tag{2.6}$$

where $v_{\mathrm{e},\theta}(r)$ is the azimuthal velocity of the electron fluid element and $E_{\mathrm{e}}(r)$ is the radial electric field.

The radial electric field produced by the space charge follows from Poisson's equation in cylindrical coordinates

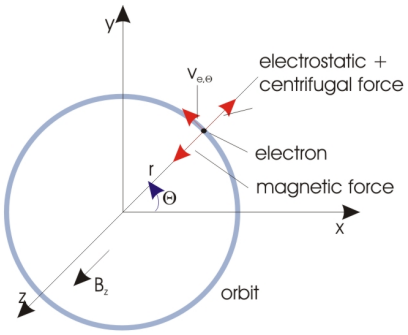

Figure 2.5: Forces Acting on an Electron Fluid Element in Steady State (Schulte 2013, p. 12)

$$\frac{1}{r}\frac{\partial}{\partial r} r E_\mathrm{r} = \frac{1}{\epsilon_0} e n_\mathrm{e}(r), \tag{2.7}$$

with $n_e(r)$ as the equilibrium density profile. Integration of equation 2.7 yields the electric field

$$E_\mathrm{r} = -\frac{e n_\mathrm{e}}{2\epsilon_0} r = -\frac{m_\mathrm{e}}{2e}\omega_\mathrm{pe}^2 r, \tag{2.8}$$

where $\omega_\mathrm{pe} = \sqrt{\frac{n_\mathrm{e} e^2}{\epsilon_0 m_\mathrm{e}}}$ is the plasma frequency. Introducing the angular velocity $\omega_\mathrm{e} = \frac{v_{\mathrm{e},\theta}}{r}$ the force balance equation 2.6 can be expressed as

$$-\omega_e^2 = \frac{\omega_\mathrm{pe}^2}{2} - \omega_\mathrm{e}\Omega_\mathrm{e}, \tag{2.9}$$

where Ω_e denotes the electron cyclotron frequency. Solving equation 2.9 for the angular rotation frequency yields

$$\omega_\mathrm{e} = \omega_\mathrm{e}^{\pm} = \frac{\Omega_\mathrm{e}}{2}\left[1 \pm \left(1 - \frac{2\omega_\mathrm{pe}^2}{\Omega_\mathrm{e}^2}\right)^{\frac{1}{2}}\right], \tag{2.10}$$

where ω_e^+ corresponds to the fast cyclotron frequencies of the electrons rotating around the magnetic field lines and ω_e^- to the slow $E_\mathrm{r} \times B_\mathrm{z}$ rotation of the complete NNP column. As the two angular velocities $\omega_\mathrm{e}^{\pm}$ are independent of the radius r the average azimuthal motion of the NNP column represents a rigid rotation around the axis of symmetry of the lens. The Brillouin density limit determines the maximum density of the NNP that can be radially confined by the magnetic field

$$n_\mathrm{e,r,max} = \frac{\epsilon_0 \mathrm{B}_\mathrm{z}^2}{2\mathrm{m}_\mathrm{e}}. \tag{2.11}$$

As the theoretical treatment of the radial confinement neglects external magnetic fields and interactions of the trapped electrons such as charge production and diffusion of particles across magnetic field lines it can only provide a maximum density but not a description of the actual space charge density confined inside the lens. Therefore there is no sufficient theory to describe the focusing characteristics of a space charge lens (Pozimski & Meusel 2005). In order to compare experimental results from different lenses the confinement efficiency κ ($0 < \kappa < 1$) is defined for the radial and longitudinal confinement (Pozimski & Meusel 2005)

$$\kappa_\mathrm{r} = \frac{n_\mathrm{exp}}{n_\mathrm{r}} \quad \& \quad \kappa_\mathrm{l} = \frac{n_\mathrm{exp}}{n_\mathrm{l}}. \tag{2.12}$$

The radial confinement κ_r is determined by the Brillouin density limit

$$\kappa_\mathrm{r} = \frac{2\omega_\mathrm{pe}^2}{\Omega_\mathrm{e}^2} = 1. \tag{2.13}$$

As the two rotational frequencies are equal in the Brillouin density limit $\omega_\mathrm{e}^+ = \omega_\mathrm{e}^- = \Omega_\mathrm{e}/2$ this state corresponds to a rigid rotation of the NNP column. The upper graph in figure 2.6 shows

the confinement efficiency κ as a function of the two rotational frequencies $\omega_e^{\pm}$. The lower three graphs show the associated motion of the electrons for different confinement efficiencies. In the case of $0 < \kappa < 1$ an individual electron confined within the NNP column experiences, under the assumption of uniformity of the space charge density, the forces produced by the self electric field E_r and the axial magnetic field B_z. The motion of the electron is defined by

$$m_e \frac{d\vec{v}}{dt} = -e(\vec{E_r} + \vec{v} \times \vec{B_z}). \tag{2.14}$$

Solving equation 2.14 and considering the electron motion in the x-y plane gives in the rotating frame of the NNP column, which is rotating with either ω_e^+ or ω_e^-, a circular gyration with a period of

$$T = \frac{2\pi}{\omega_e^+ - \omega_e^-}. \tag{2.15}$$

In the Brillouin density limit this circular gyration vanishes because ω_e^+ and ω_e^- are identical. $\kappa = 0$ represents the case of complete neutralization. The neutralization is due to the fact that ions created inside the lens, by electron impact ionization, will form a neutralizing background for the NNP column despite their extraction from the lens by the positive anode potential. In the case of complete neutralization the axial magnetic field acts only on the electrons and consequently the NNP column no longer performs a $E \times B$ rotation.

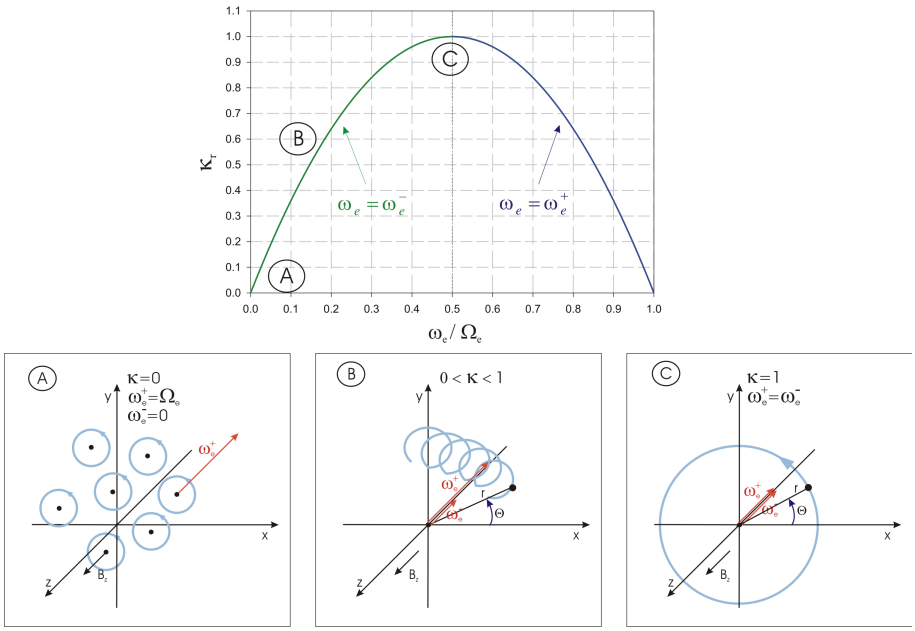

Figure 2.6: Upper Graph: Confinement Efficiency as a Function of the Two Rotational Frequencies Lower Graphs: Associated Motion of the Electrons (Schulte 2013, p. 14)

Longitudinal Confinement

The electrode system produces a potential well in longitudinal direction. The depth of the potential well is defined by the potential of the anode ϕ_A and is reduced by the potential of the space charge ϕ_r, as shown in figure 2.7.

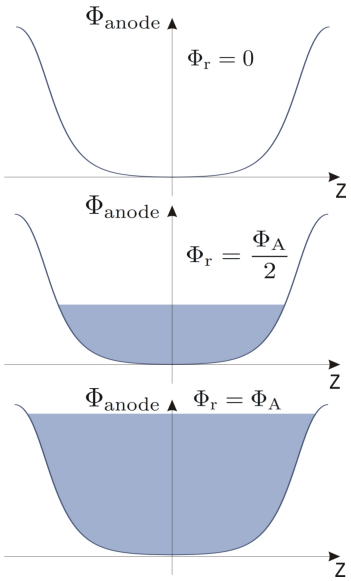

Figure 2.7: Potential Well ϕ_A Created by the Electrode System and Space Charge Potential ϕ_r (Schulte 2013, p. 10)

Under the assumption of a cold and homogeneously distributed NNP column, the space charge potential ϕ_r is given by the radial electric field E_r

$$\phi_r(r) = -\int_0^{R_A} E(r)\mathrm{d}t, \tag{2.16}$$

where R_A denotes the radius of the cylindrical anode. In the case of a complete potential depression $\phi_A = \phi_r$ the maximum space charge density in longitudinal direction is reached

$$n_{e,l,max} = \frac{4\epsilon_0\phi_A}{eR_A^2} \tag{2.17}$$

and the longitudinal confinement efficiency is

$$\kappa_l = \frac{n_{exp}}{n_{e,l,max}}. \tag{2.18}$$

As discussed in the previous chapter it is impossible to theoretically determine the space charge density of a Gabor lens prototype due to the omission of effects associated with the interaction of the trapped electrons in general. In the case of the longitudinal confinement an additional difficulty is the determination of the radial expansion of the space charge cloud, which influences the maximum space charge density.

Focussing Principle

The Gabor lens makes use of the radial self electric field produced by a non-neutral electron plasma column to focus positively charged ion beams. In the case of a homogeneous electron distribution inside the lens it can be assumed that a radial focussing force $F_r = q_{ion}E_r$ acts on the incoming ions with charge q_{ion}. If both confinement conditions equation 2.11 and equation 2.17 are simultaneously fulfilled a relation between the potential of the anode, the magnetic field and the anode radius can be derived (Reiser 1989):

$$\phi_A = \frac{eR_A^2}{8m_e}B_z^2. \tag{2.19}$$

Using the equation of motion for a single proton which enters the lens with charge q_p, mass m_p and a longitudinal velocity $\vec{v_p}$ and the thin lens approximation the focal lens f_{GL} of a Gabor lens can be derived for protons

$$\frac{1}{f_{GL}} = \frac{e}{8m_e}\frac{B_z^2}{U_B}l, \tag{2.20}$$

where $U_\mathrm{B} = \left(\frac{m_\mathrm{p} v_\mathrm{p}^2}{2q_\mathrm{p}}\right)$ is the total accelerating potential of the protons and l the effective length of the Gabor lens (Pozimski & Aslaninejad 2013).

2.2.2 Electron Production

Additionally to the confinement of the space charge the electron production in the Gabor lens is a crucial aspect in order to generate a stable and homogeneously distributed NNP. Three different mechanisms have been proposed for the production of electrons. In his original publication Gabor proposed the use of a hot cathode for the production. A hot cathode on the one hand is able to produce a lot of electrons but on the other hand the electrons are only produced locally, which makes the correct positioning of the cathode and the generation of a homogeneously distributed NNP difficult. To distribute the electrons homogeneously the magnetic field lines which run through the centre of the lens can also be let through the region of electron production (Pozimski 1990, p. 36) but this would increase the requirements on the design of the magnetic fields and in combination with optimizing the position of the cathode would increase the constructional work significantly.

The second proposed mechanism is to use the ionization of residual gas atoms by electrons and residual gas ions for the production. For this mechanism an electron, for example produced by cosmic radiation, is accelerated inside the lens due to the electric field and ionizes residual gas atoms in the lens. This leads to an increasing number of electrons, which can ionize further gas atoms. To theoretically describe the ignition of a NNP through residual gas ionization Paschen's law with the restriction to electrons produced by residual gas ionization can be used. Due to the restriction the second Townsend coefficient γ_se is neglected, which represents the production of secondary electrons on metal surfaces. This leads to the modified Paschen's law for the ignition of NNPs

$$V_\mathrm{B} = \frac{Bpd}{\ln(Apd)}, \tag{2.21}$$

where V_B is the breakdown voltage for the ignition, A and B are experimentally determined gas constants, p is the pressure inside the Gabor lens and d is the distance given by the crossed configuration of electric and magnetic fields (Schulte 2013). Similar to the space charge production by a hot cathode the position of the NNP ignition is important. Generally, it is expected that the ignition happens between the cylindrical anode and the ground electrode but in practice if the Gabor lens is operated on the left side of Paschen's minimum the NNP does not ignite between the electrodes (Pozimski 1990).

The residual gas ionization by the incoming ion beam is the third mechanism to produce the space charge. This process is independent from the other two mechanisms and the construction of the Gabor lens and naturally occurs when the lens is used for ion capture and focussing. It's advantages are that the electrons are created close to the ion beam and over a large region which is crossed by many magnetic field lines. It therefore increases the chances of generating a homogeneously distributed space charge in the lens' volume. Considering the advantages and disadvantages of the individual mechanisms the Gabor lens prototype at Imperial College London was build without a hot cathode due to the constructional costs. Hence the NNP is produced by residual gas ionization by electrons and residual gas atoms and in the case of a beam test also by the beam ions.

2.3 Imperial College London's Gabor Lens Prototype

2.3.1 Summary of Previous Beam Tests

In 2015 the Gabor lens built by Imperial College London was tested in a proton beam experiment at University of Surrey. Figure 2.8 shows a schematic overview of the experiment, in which the Gabor lens was supposed to focus the incoming proton beam. During these first experiments the Gabor lens unexpectedly converted the incoming pencil beams (1 MeV) into rings with different radii depending on the lens settings. The centre of the rings was different from the initial position of the proton pencil beams, making a purely geometrical explanation of their occurrence impossible and identifying a time-dependent effect as source. Furthermore, periodic features along the circumference of the ring were observed, suggesting that the NNP was burning in an unstable state. The data analysis of the beam experiment concluded that due to the geometry of the lens a coherent off-axis rotation of the NNP is the only possible explanation for the creation of the

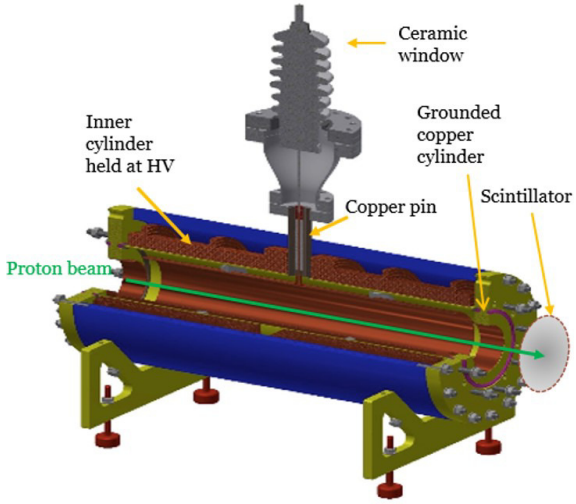

Figure 2.8: Schematic Overview of Beam Test at University of Surrey (Posocco et al. 2016)

rings (Posocco et al. 2016). Figure 2.9 shows the circular shaped proton beams observed on the scintillator for different coil currents and that the diameter of the rings increased with the coil current. The electrode system was operated at voltages between 10 and 24 V and the solenoid

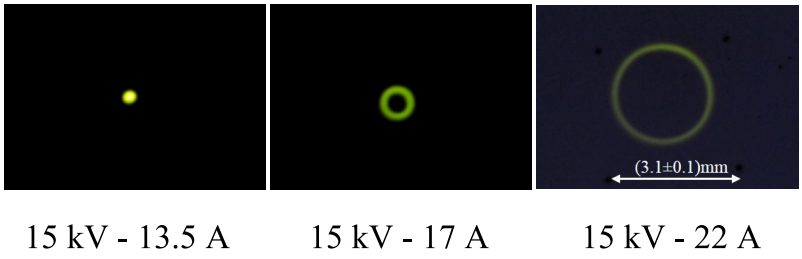

Figure 2.9: Circular Shaped 1 MeV Proton Pencil Beam as Observed on the Scintillator (Posocco et al. 2016)

at currents between 14 and 23 A while the pressure inside the lens was kept at 10^{-6} mbar. To avoid the conversion of the beam into rings possible causes for instabilities within the NNP were removed. Hence, the configuration of the magnetic coils was improved, the pressure was reduced to 10^{-7} mbar and regions of stable NNP were identified. In a second proton beam experiment at University of Surrey in 2017 the results confirmed that the measured circles produced by the Gabor lens haven't been affected by the changes but that they are inherent in the design of the lens and that they are not caused by the experimental setup of the lens (private communication with Dr. Pozimski). The hypothesis to explain the behaviour is that an electron bulk is formed in the NNP and that its off-axis rotation displaces the incoming proton beam from its initial position and drags it into a circular shape. The off-axis rotation of the NNP could be explained by a mismatch of the symmetry axis of the cylindrical Gabor lens and the radial magnetic field, i.e. the symmetry axis of the magnetic field does not lie on top of the one of the Gabor lens but encloses an angle with it. To support the hypothesis of a rotating electron bulk a measurement of the $E \times B$ induced rotation frequency of the NNP would be an elegant starting point as it is not possible to measure the frequency of a rotating, homogeneous NNP. For a homogeneous NNP the electromagnetic wave caused by the movement of electrons on one side of the lens is cancelled out by the opposite movement of electrons on the other side. Hence, a rotation frequency measurement would demonstrate that the NNP confined within the lens is inhomogeneous, supporting the hypothesis of a rotating electron bulk.

In this work two experiments for NNP diagnostics are proposed. The radio frequency (RF) emission measurement for detecting an electromagnetic wave potentially emitted by a rotating electron bulk and the RF-transmission measurement for obtaining information about the density of the NNP. Chapter 2.4 and chapter 2.5 provide an overview of the design and the underlying

theory of the two experiments. In chapter 3 the conducted experiments are presented and discussed.

2.3.2 Gabor Lens Setup and Operation Principle

Figure 2.10 shows the general setup of the Gabor lens which was used for the rotation frequency measurements. It consists of

1. Gabor lens with electrode system and solenoid
2. Roughing pump (Edwards 5)
3. Turbo molecular pump (Leybold Turbovac 151)
4. Power supply (Glassman LP 60-46)
5. High voltage supply (Glassman Series FR)
6. Water cooling system (Betta CU700)
7. Pressure gauge (Leybold Penninvac PTR 90 N)
8. Pessure gauge monitor (Leybold Graphix One)
9. Three vacuum valves (Edwards Speedivalve and Leybold Lock Valve)
10. Turbo molecular pump controller No. 3 (not in figure 2.10).

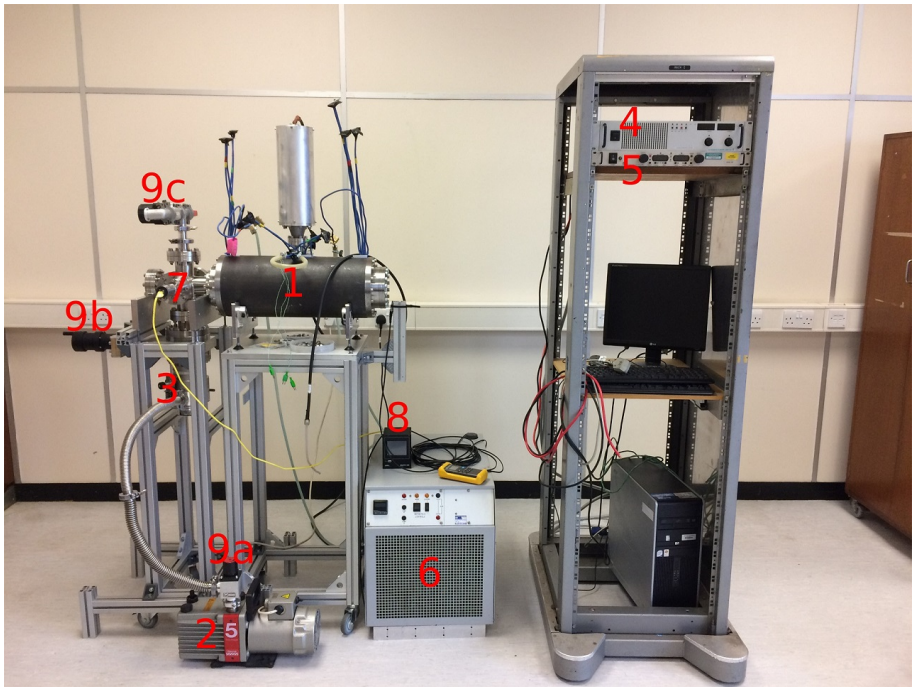

Figure 2.10: The General Gabor Lens Setup and Its Components

In a first step to generate a NNP, which is feasible of proton focussing, the setup is pumped down to 10^{-7} mbar using the roughing pump and the turbo molecular pump. A two level pump station is required because the turbo molecular pump must only be switched on when a pressure of 10^{-1} mbar is already established. In a second step the cooling system is turned on to prevent the solenoid from getting to hot, which would increase the pressure in the lens. In a third step the power supply is used to regulate the current, which flows through the solenoid. Typical values for the current lie between 15 A and 30 A. In a fourth step the high voltage supply provides the voltage for the electrode system to generate the potential well, typical values lie between 8 kV and 20 kV. If a NNP is established, the pressure and the current displayed on HV supply rise approximately by a factor of 5 to 10 and 10 μV.

2.4 Model of Electric- and Magnetic Fields Inside the Gabor Lens

The electric and magnetic fields inside the Gabor lens were modelled with COMSOL Multiphysics, a software that solves coupled systems of differential equations with finite element analysis. For this project the existing models of the Gabor lens were used to calculate the $E \times B$ induced rotation frequency of the NNP column. The models only differ in the boundary condition for the magnetic fields. An overview of the three models can be found in table 2.4. The models correspond to different operation modes of the Gabor lens prototype, which determine the state of the NNP. The model-30-20 corresponds to the state in which the maximum electron density is confined within the Gabor lens. In the model-30-25 the coil current of 25 A produces such a strong radial magnetic field that electrons are lost. Hence, this model exhibits an inhomogeneous electron density. The

Table 2.4: Gabor Lens Models

Model	Anode Voltage	Coil Current
Model-30-15	20 kV	15 A
Model-30-20	20 kV	20 A
Model-30-25	20 kV	25 A

rotation velocity v_{rot} in dependence of the radius r was calculated for the three models according to

$$v_{\mathrm{rot}} = \frac{E_{\mathrm{r}}}{B_{\mathrm{z}}}. \tag{2.22}$$

Relation

$$f_{\mathrm{rot}} = \frac{v_{\mathrm{rot}}}{2\pi r} \tag{2.23}$$

was used to to obtain the frequency f_{rot} of the rotation. Figure 2.11 shows the modelled electric and magnetic fields used for the calculation and figure 2.12 shows the expected frequencies for three models. The x-axis in all plots represents the line, which lies in the longitudinal middle of the lens, starts at symmetry axis of the lens and ends at the grounding. The slight decrease of the magnetic field towards larger radii can be explained by the construction of the lens, i.e. the magnetic field is plotted along the line where the solenoid is split by the HV feedthrough, see figure 2.11b. The radial electric fields behave as expected in the 15 A and 20 A model, i.e. they increase linear with the radius, see figure 2.11a. In the 25 A model the radial electric field exhibits a non-linear behaviour, which can be explained by the inhomogeneity of the electron density.

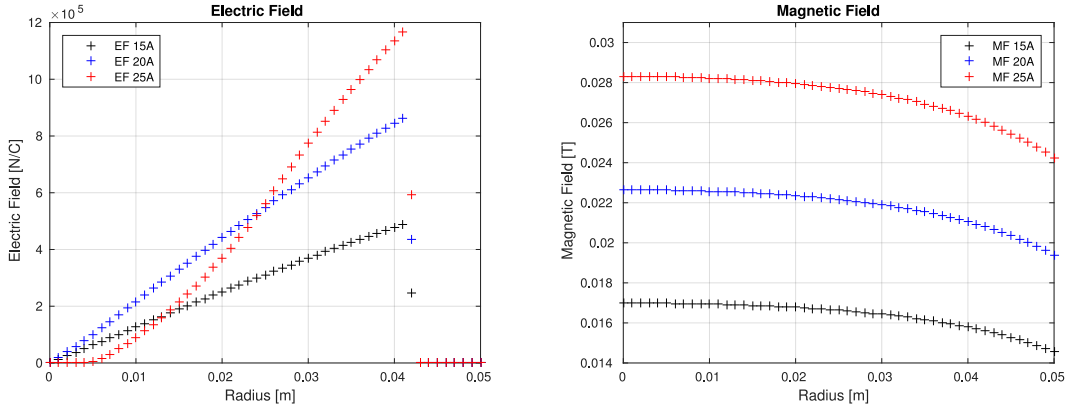

(a) Electric Field

(b) Magnetic Field

Figure 2.11: Simulations on the Electric and Magnetic Fields

Inserting equation 2.22 into equation 2.23 and setting

1. $B_{\mathrm{z}} = B_0$

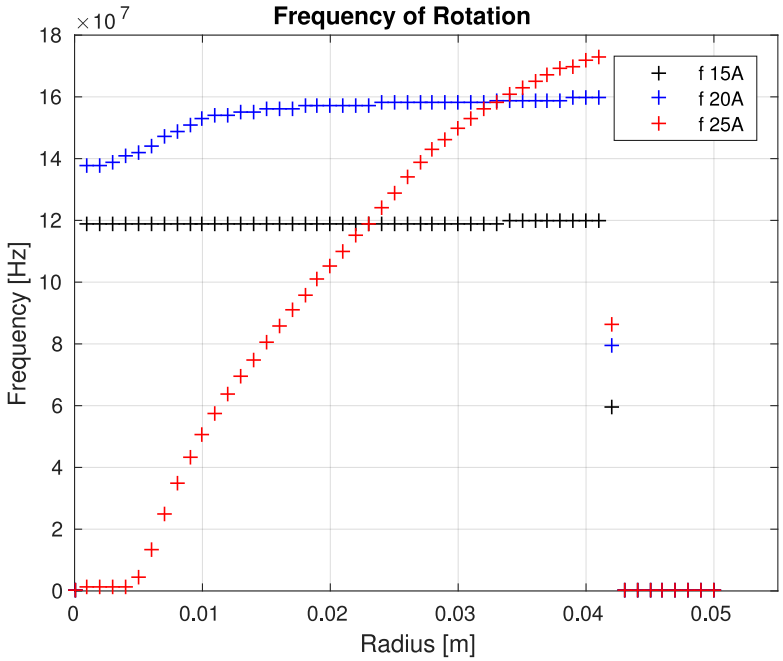

Figure 2.12: Rotation Frequencies for the Three Gabor Lens Models

2. $E_r = E_0 r$,

with constants B_0 and E_0 gives a relation for the behaviour of the rotation frequency

$$f_{\text{rot}} = \frac{E_0}{2\pi_0}. \tag{2.24}$$

This explains why the behaviour of the frequency differs for the three cases. The highly linear radial electric field in the 15 A model corresponds to a constant rotation frequency, where as the non-linearities of the radial electric field in the 25 A model cause a wide range of expected frequencies. Previous experiments showed that the most promising NNP state for focussing protons is established at a coil current of 25 A, hence RF-measurements were designed to measure a frequency in the range of 1.12 MHz to 173 MHz.

2.5 NNP Diagnostics with RF Antennas

As the calculations in chapter 2.4 showed $E \times B$ induced rotation frequencies between 1.12 MHz and 173 MHz can be expected. In the case of a rotating electron bulk a circular polarised electromagnetic wave will be emitted and in principal this signal should be detectable with RF-antennas.

2.5.1 Antenna Fundamentals

This section summarizes a few of the fundamental concepts for the correct design and use of RF-antennas. It mainly follows the argumentation of the book Practical digital wireless signals (McCune 2010). Antennas are the transducer between electronic signals and propagating electromagnetic fields, i.e. they convert energy from a propagating electromagnetic wave into an electronic signal and vice versa. Therefore, antennas can be used for both sending and receiving an electromagnetic field and their reciprocity ensures that they have the same characteristics for both processes. The efficiency of this process is called the antenna radiation efficiency η and is defined as

$$\eta := \frac{P_T}{P_R}, \tag{2.25}$$

where P_T is the power of the electromagnetic field and P_R is the power of the electronic signal. Antennas are also resonant devices, i.e. their physical length relates to the wavelength λ of the

radiated or received signal. When designing antennas for a specific measurement it is crucial to take both the radiation efficiency and the relation between physical length and wavelength into account. Therefore the following aspects were considered for the design of the RF-antennas used in the RF-emission and transmission measurements.

Polarization

For electromagnetic waves the direction of the oscillating electric field component relative to the direction of propagation defines the polarization. Similarly, antennas have a polarization which is defined by their structure and its orientation relative to the ground, i.e. a vertically mounted wire antenna is vertically polarized and a horizontally mounted one is horizontally polarized. The most common types of polarization and corresponding examples of antenna types are shown in figure 2.13. For the sending antenna the polarization of the antenna defines the polarization of the emitted signal. To avoid signal losses the polarization of the receiving antenna has to be matched to the polarization of the incoming signal because antennas are most responsive to signals of the same polarization. But even if the receiving antenna matches the polarization of the emitted signal this does not prevent the electromagnetic wave from changing its polarization while propagating due to reflections and consequently reducing the measured signal strength.

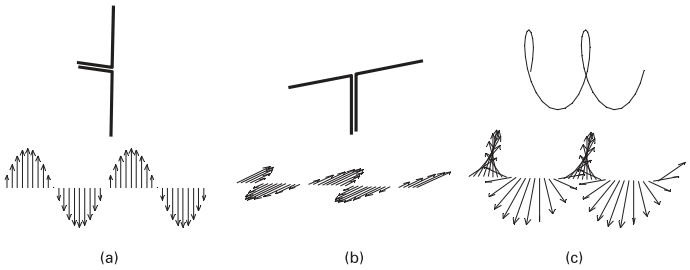

Figure 2.13: Common Types of Polarization and Corresponding Antenna Types: a) vertical, b) horizontal and c) circular (McCune 2010, p.255)

Bandwidth

As antennas are resonant devices they operate best at their resonance frequency. A common type of monopole antenna is the $1/4$ wavelength antenna because it is shorter than the full wavelength antenna but still resonant. Even though antennas operate best at their resonance frequency they are also able to detect other frequencies. The bandwidth expresses in which frequency range around the resonance frequency an antenna still operates well and is commonly defined as the range in which the power gain is maintained to within 3 dB of its maximum (Aragon-Zavala 2008).

Near and Far Field

The distinction between near and far field is directly connected to the physical size of the antenna. In the radiating far field the distances from all positions on the antenna to the measuring point are approximately equivalent. In the case of the radiating near field the distances to different positions on the antenna are significantly different, so that wave phase contributions from these positions will vary with the distance from the antenna. The boundary between near and far field is not well defined in the literature but is suggested at a radius $R = \frac{2\mathrm{D}^2}{\lambda}$, with D as the diameter of the antenna, for physically large antennas, i.e. larger than a half-wavelength of the radiation they emit. For physically small antennas the suggestions vary from $R = \frac{2D^2}{5\lambda}$ to $R = \frac{2D^2}{10\lambda}$. As the prototype monopole antennas build for the RF-measurements are limited to a length of 5 cm by the diameter of the lens and are therefore physically small the boundary is supposedly at 0.13 μm or 0.07 μm for $D = 1$ mm and a 100 MHz signal. Hence, all of the RF-measurements were conducted in the radiating far field.

2.5.2 Self Build Antennas

In a first step to measure the expected RF-signal two linear polarized monopole antennas were build by the electrical workshop out of a 50 Ω cable, see figure 2.14a. Due to the fact that the

(a) Self-Build Antenna 1 and 2

(b) Taoglas CA.69 Antennas

Figure 2.14: RF-Antennas

antennas were build out of a 50 Ω cable their impedance is 50 Ω and matches with impedance of the cables and each other. In the case that the impedances of the individual do not match reflections of the signal on the transitions would occur. Ideally, at least a quarter-wavelength monopole antenna should be used to ensure a broad bandwidth and good efficiency. Hence, the self-build antennas are not ideal for the detection of RF signals but should nevertheless be able to measure strong signals emitted by the rotating electron bulk. Additionally, two commercial CA.69 antennas (taoglas antenna solutions, Enniscorthy, Ireland) were purchased and soldered to two 50 Ω cables, see figure 2.14b. Their specifications are listed in table **??**. These CA.96 antennas supplement the self-build antennas with a centre frequency at the upper end of the expected signal and a small bandwidth.

2.5.3 Test Setup for Characterization of Self-Build Antennas

To characterize the two self-build antennas a function generator (Tektronix AFG 3251) and a digital phosphor oscilloscope (Tektronix DPO 3014) were used to transmit a signal between the antennas and to evaluate it. For this purpose antenna 2 was connected to the function generator with a 50 Ω cable and antenna 1, mounted in a distance from antenna 2, was connected to the oscilloscope using another 50 Ω cable, see figure 2.15. For these experiments the distance between the antennas, the frequency of the generated function and the orientation of the antennas to each other (parallel and orthogonal) were varied. The orientation of the antennas is important as it determines the polarization of the antennas and the RF-signal, i.e. vertical or horizontal and therefore influences how well a signal can be transmitted. All these experiments were carried out in air and with no objects directly in between the antennas to study the basic properties of the experimental setup and its components. In later experiments on the burning NNP further aspects such as deflections of the signal and propagation of it through a circular waveguides will make the measurements more complex. For all measurements with the test setup the settings of the function generator were a sine function with an amplitude of 5 V_{pp}, a phase of 0° and an offset of 0 mV. The sensitivity of the oscilloscope was set to 1 mV. During the measurements a FFT was performed on the oscilloscope using different window functions.

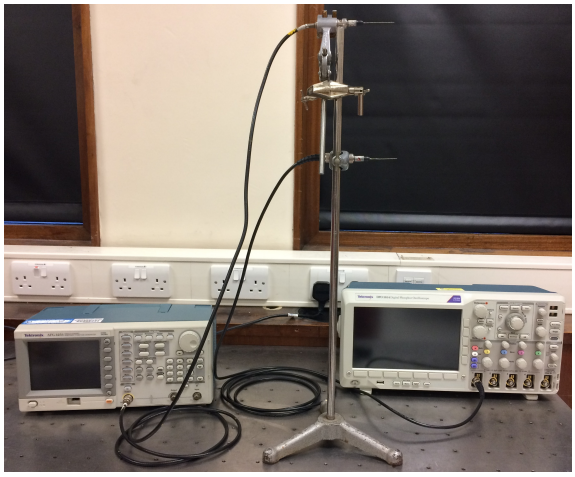

Figure 2.15: Antenna Test Setup for Self-Build Antennas

2.5.4 Setup for NNP Diagnostics

To detect a RF-signal emitted by the NNP two types of measurements were designed. The first type is supposed to directly measure the RF-signal emitted by the NNP and is called the RF-emission experiment. For this purpose a crossed configuration of the two self-build antennas was installed as close to the vacuum window as possible to minimize losses due to distance from the emitting NNP, see figure 2.16. The vertical antenna was connected to channel one of the oscilloscope and the horizontal antenna to channel two. The idea of the crossed configuration of two linear polarized antennas is, that on the one hand side both of the antennas should theoretically detect the same amplitude in signal from a circular polarized wave emitted by the NNP and on the other hand side detect different linear polarized signals from background sources, depending on their orientation. This improves the discrimination of signal coming from the NNP from signals produced by external sources, as only signals detected by both antennas need to be considered as potential rotation frequency. For the second type of measurements a CA.69 antenna was installed on the other side

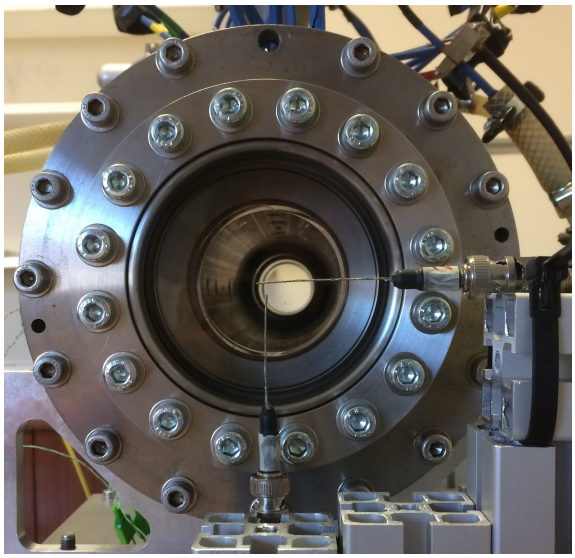

Figure 2.16: Crossed Configuration of Self-Build Antennas

of the Gabor lens in a 45 degree angle to both antennas in the crossed configuration, see figure 2.17. This setup is called the RF-transmission measurement. The additional antenna was used to send a signal generated by the function generator through the Gabor lens to determine the influence of the NNP on the transmitted signal and gain information about the NNP density. Because of the linear polarization of the taoglas antenna the angle of 45° was chosen in order to provide equal signal strength for both receiving antennas. If the sending antenna is installed in

either a vertical or horizontal position one of the receiving antennas would be favoured over the other and consequently receive more signal. In order to suppress background noise and to prevent

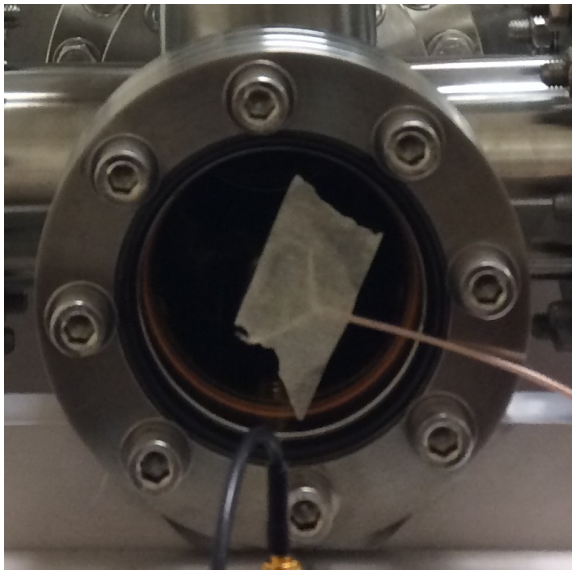

Figure 2.17: A CA.69 Antenna as Sending Antenna

the signal emitted from the CA.69 antenna from travelling around the Gabor lens to the self-build antennas a shielding around the crossed configuration of antennas was build. The shielding consists of a plastic cylinder covered in double-layered aluminium foil and a cooper hat. It was directly mounted on the vacuum window, connected to the ground of the Gabor lens and has two holes for the self-build antennas, see figure 2.18.

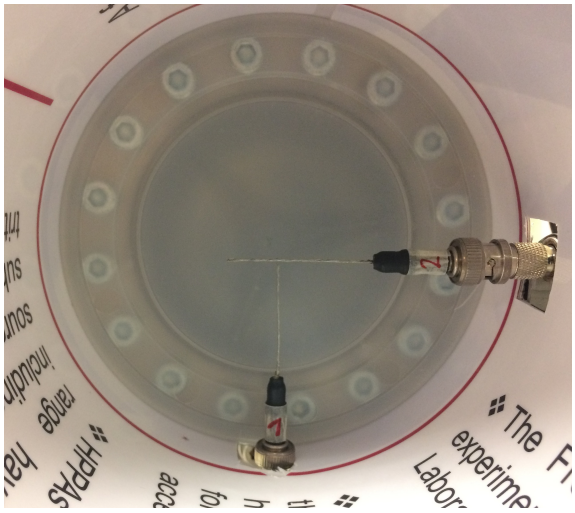

Figure 2.18: Shielding of Self-Build Antennas in Crossed Configuration

The complete setup used for NNP diagnostics is shown in figure 2.19. The following components were added compared to the general Gabor lens setup: function generator, oscilloscope, shielding.

2.5.5 Data Analysis

The data analysis of the RF-measurements was conducted in two steps. As first step the signal measured during the experiments was directly transformed into the frequency domain using the Fast Fourier Transformation (FFT) of the oscilloscope. The oscilloscope's FFT offers different possible window functions, which were used to optimize the data analysis. This made a direct evaluation of the results and an optimization of oscilloscope parameters such as acquisition mode,

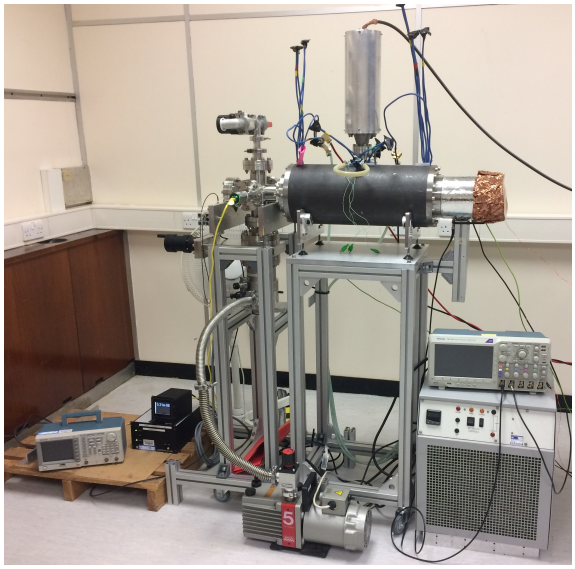

Figure 2.19: Gabor Lens Setup for NNP Diagnostics

record length and sensitivity during the measurement possible. It also revealed that moving an office chair close to the setup induced a signal with significant amplitude in the range of the expected rotation frequency. In a second step all the pre-settings, measurements and FFTs of the oscilloscope were saved to an usb-stick and analysed in MATLAB. MATLAB was used for the removal of the DC-component of the signal, FFT of the spectra, implementation of different window functions, measurement of the peak hight and plotting of the graphs. MATLAB computes the discrete Fourier transformation (DFT) defined as

$$Y(k) = \sum_{j=1}^{n} X(j) W_n^{(j-1)(k-1)}, \tag{2.26}$$

where $W_n = \mathrm{e}^{(-2\pi \mathrm{i})/n}$ is one of n roots of unity using a fast Fourier transform (FFT) algorithm (MathWorks 2018). Moreover, MATLAB was used to detect peaks in the amplitude spectrum, with a height above a certain threshold, and to label them.

Chapter 3

Results & Discussion

3.1 Simulations on the Penetration Depth of Ions Through Matter

The necessary energies for the different ions to pass the boundary at 14.43 mm of skin cell type 1 monolayer and the polyethylene layer are summarized in table 3.1.The results show, that for ions heavier than protons, the necessary energy of the ions to pass through the cell monolayer considerably increases. The results for the simulations on the penetration depth of different ions in

Table 3.1: Results of Simulations for Different Ions

Ion	Energy (MeV/ion)	Energy (MeV/u)	Mean range (mm)	Straggling (μm)
H-1	5	5	14.5	145.00
He-4	21	5.25	14.5	3.35
Li-7	42	6	14.5	2.63
C-12	109	9.08	14.5	1.63

water are summarized in table 3.2. In the first four rows the magnetic rigidity for H-1, He-3, He-4 and C-12 are compared for an identical penetration depth of 5 cm. Rows five and six compare the penetration depth of He-4 and C-12 for a given magnetic rigidity of 45.6 nTm.

Table 3.2: Penetration Depth of Ions in Water with SRIM

Ion	$B\rho$ (nTm)	E (MeV/ion)	E (MeV/u)	Mean range (mm)	Straggling (mm)
H-1	87.9	79	79	50.00	0.70
He-3	1.52	273	91	50.00	0.40
He-4	1.72	310	77.5	50.00	0.70
C-12	3.23	1,740	145	50.00	0.20
He-4	45.6	82	20.5	44.40	0.30
C-12	45.6	246	20.5	15.00	0.00

These simulations show that for the same penetration depth heavier ions than protons are a more resistant to external magnetic fields. In the case of the given magnetic rigidity for He-4 and C-12 the He-4 beam has a deeper penetration depth. For these simulations L. Murgatroyd compared the results obtained by SRIM to BDSIM simulations with a Gaussian beam distribution and found good agreement even though the values are not identical. The small discrepancies might be explained by the fact that for the SRIM simulations the beam distribution is unknown and hence might not be Gaussian shaped. The BDSIM results are listed in table 3.3.

Table 3.3: Penetration Depth of Ions in Water with BDSIM

Ion	$B\rho$ (nTm)	E (MeV/ion)	E (MeV/u)	Mean range (mm)	Std. Deviation (mm)
H-1	87.9	79	79	50.90	0.50
He-3	1.52	273	91	49.30	0.30
He-4	1.72	310	77.5	49.50	0.30
C-12	3.23	1,740	145	50.10	0.20
He-4	45.6	82	20.5	45.00	0.00
C-12	45.6	246	20.5	15.00	0.10

Discussion

In the case of the investigations of the energy losses of ions in the radiobiological endstation the results indicate that with the setup assumed for the simulations cell irradiations with laser-accelerated ions heavier than protons are significantly increasing the requirements and consequently the costs of the laser system. In the case of the investigations on the magnetic rigidity of the different ion beams the results indicate that for ions heavier than protons the ion beams are much more resistant to deflection and therefore stronger and more expensive magnets would be needed to bend their beam. This would also considerably increase the overall costs of an irradiation facility capable of handling various ion types.

3.2 Imperial College London's Gabor Lens Prototype

3.2.1 Assembly and Connection to the Cerberus Laser System

As a first step towards radiobiological experiments with laser accelerated ions the Gabor lens prototype was connected to Imperial College London's Cerberus laser system, which generates multi-TW laser pulses and focuses them on target foils or gas jets to produce various ions. The setup consists of the components, which are listed in chapter 2.3.2 except the water cooling system. Additionally added were the Cerberus laser system, a fan, the Medusa particle detector and a scintillator screen. Figure 3.1 shows the setup starting with the Cerberus laser system (1) on the left hand side, followed by vacuum valve 9b (2), the Gabor lens (3), vacuum valve 9c (4), the turbo molecular pump (5), the vacuum gauge (6), a fan (7), the Medusa particle detector (8) and the scintillator screen on the right hand side. The roughing pump, high voltage supply, power supply, pressure gauge monitor and the turbo molecular pump controller. While pumping the laser system and the Gabor lens individually, i.e. valve 9b (2) was closed, it became clear that neither the Cerberus laser system nor the Gabor lens could be brought down to a pressure of 10^{-7} mbar. The pressure inside the Gabor lens levelled out at 3.4×10^{-6} mbar. Nevertheless, the ignition of a NNP inside the lens was successful and flashes of light were visible on the scintillator screen.

Discussion

After the first beam test at University of Surrey in 2015 the vacuum system of the Gabor lens was improved such that a pressure of 10^{-7} mbar was achieved in the system. The second beam test in 2017 showed that this improvement did not prevent the lens from converting an incoming proton pencil beam into a circular shape on the scintillator but it allowed to identify regions of stable NNP. With a pressure in the range of 10^{-7} mbar regions of stable NNP can be clearly distinguished from regions of unstable NNP. For higher pressures this distinction is more difficult and requires a lot of experience. Hence, for a stable operation of the Gabor lens in future beam experiments the reason for the rise in pressure has to be identified and resolved. Probable causes for the increase are outgassing and a vacuum leak.

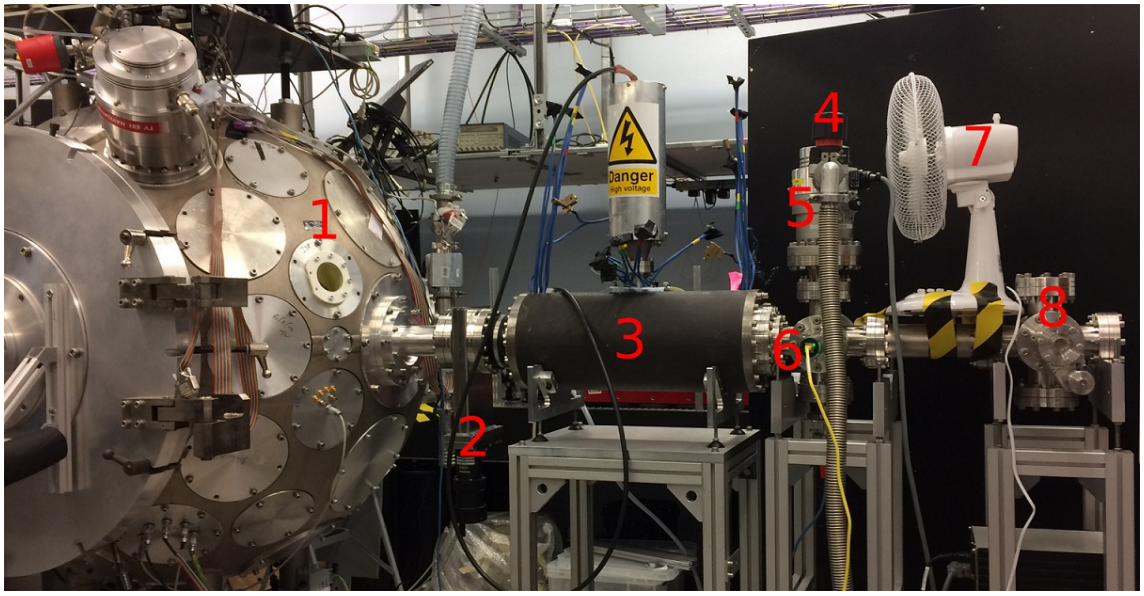

Figure 3.1: The Cerberus Laser System Connected to the Gabor Lens

3.2.2 Modification of the Gabor Lens setup and Vacuum Diagnostics

In order to perform vacuum diagnostics the setup of the Gabor lens was modified. The Medusa particle detector was removed, all flanges were cleaned with ethanol and securely locked. Additionally, the scintillator was removed and both ends of the system were equipped with glass vacuum windows for future RF-measurements on the Gabor lens. Figure 2.10 from chapter 2.3.2 shows the setup. After the setup was modified the system was pumped over the duration of twelve days (31.05.18 - 11.06.18) with short interruptions for further improvements and vacuum diagnostics until the pressure levelled out at 2.83×10^{-6} mbar. For the vacuum tests valve 9b was closed, isolating the lens from the pumps, which caused a significant rise in pressure in the lens. To determine if this behaviour is due to outgassing or a leak the lens was isolated over the duration of 65 minutes and the rise in pressure was recorded with the pressure gauge. The pressure rose from 2.83×10^{-6} mbar to 7.24×10^{-3} mbar and dropped back to 2.83×10^{-6} mbar within 15 minutes after closing valve 9b again. Figure 3.2 shows the linear trend of the rise in pressure. The jump in pressure after 575 seconds is due to the switching of the pressure gauge from one sensor to another. The gauge uses thermal conductivity and cold cathode ionization as measurement principles to cover the full range from 10^{-8} mbar to atmosphere.

Discussion

Removing parts of the system, which are not needed for RF-measurements, and cleaning and checking all valves reduced the pressure by 0.57×10^{-6} mbar compared to the pressure achieved during the connection to the Cerberus laser system. But the modifications did not eliminate the main cause of the increased pressure in the system. The linear rise in pressure in figure 3.2 identifies a leak as the main source for the increased pressure. In case of outgassing as main source the pressure would have saturated during the vacuum test. Due to the small size of the leak a dedicated helium leak detector would be required for a precise localization.

3.3 NNP Diagnostics with RF-Antennas

3.3.1 Characterization of the Self-Build Antennas

As preparation for the RF measurements on the confined NNP the self-build antennas were tested in order to characterize their behaviour in different configurations and to characterize the background noise present in the accelerator lab (room 537, Blackett Building). For this purpose the test setup and the settings for the oscilloscope and the function generator from chapter 2.5.3 were used. All graphs in this chapter are based on the FFT provided by the oscilloscope and were plotted

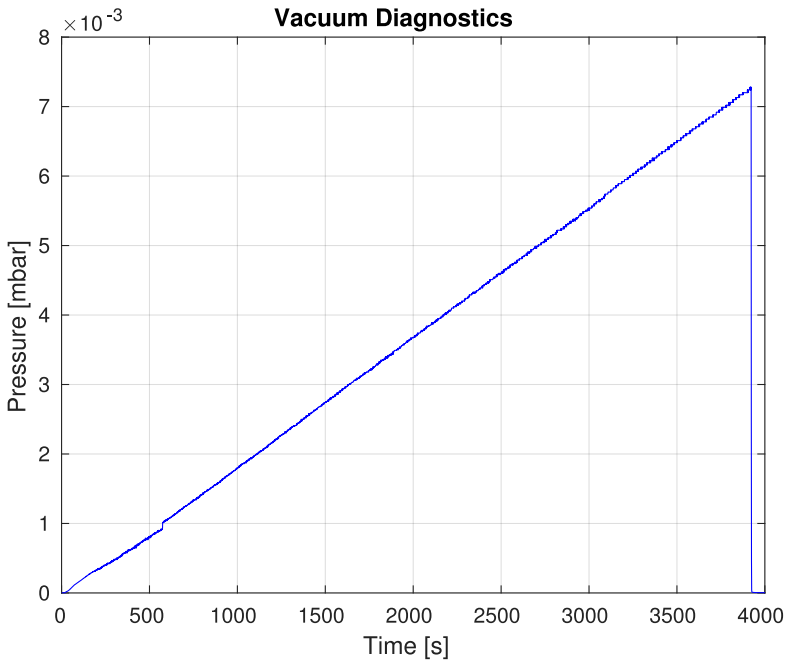

Figure 3.2: Vacuum Diagnostics

with MATLAB. The oscilloscope's FFT offers a range of window functions each optimized for a certain purpose. The rectangular window is best at resolving frequencies and worst at measuring the amplitude of those frequencies. The Blackman-Harris window on the other hand is best at measuring the amplitudes but worst at resolving the frequencies (Tektronix 2012*b*, p. 114 & 115). The performance of all other window functions lie in between these two. The Blackman-Harris window was used for all sections in chapter 3.3.1.

Noise Measurements

In order to interpret the amplitude spectra of later RF-measurements on the confined NNP correctly it is important to understand how the background noise of the experimental setup behaves. If the noise is well understood frequencies coming from the NNP can be distinguished from frequencies related to other external sources and contributions inherent in the design of the experiment. To estimate the influence of noise on the measured signal two different noise measurements were performed using the setup, which was described in chapter 2.5.3. For the Grounded Background measurement (GBM) channel 1 of the oscilloscope was covered with a 50 Ω cab and additionally internally grounded. For the Background of Setup measurement (BSM) antenna 1 was connected to the function generator with turned off output and antenna 2, mounted in parallel in a distance of 12 cm, was connected to channel 1 of the oscilloscope. Fig. 3.3 shows the amplitude spectra of these two noise measurements in comparison with a spectrum measured for a sine wave at 100 MHz generated by the function generator. Figure 3.3 shows that the spectrum of the GBM exhibits seven peaks, which are labelled from low to high frequencies. These peaks have to be explained and taken into account for further measurements. Peak 1 at the beginning of the spectrum represents the DC component of the signal and peak 7 at the end of the spectrum is an artefact of the FFT. The peaks 2 till 6 in between these two are up to 18 dBV higher than their surrounding frequencies. Table 3.4 lists these five frequencies and their amplitude. Additionally, lower frequencies till 100 MHZ generally exhibit a larger amplitude than frequencies over 100 MHz.

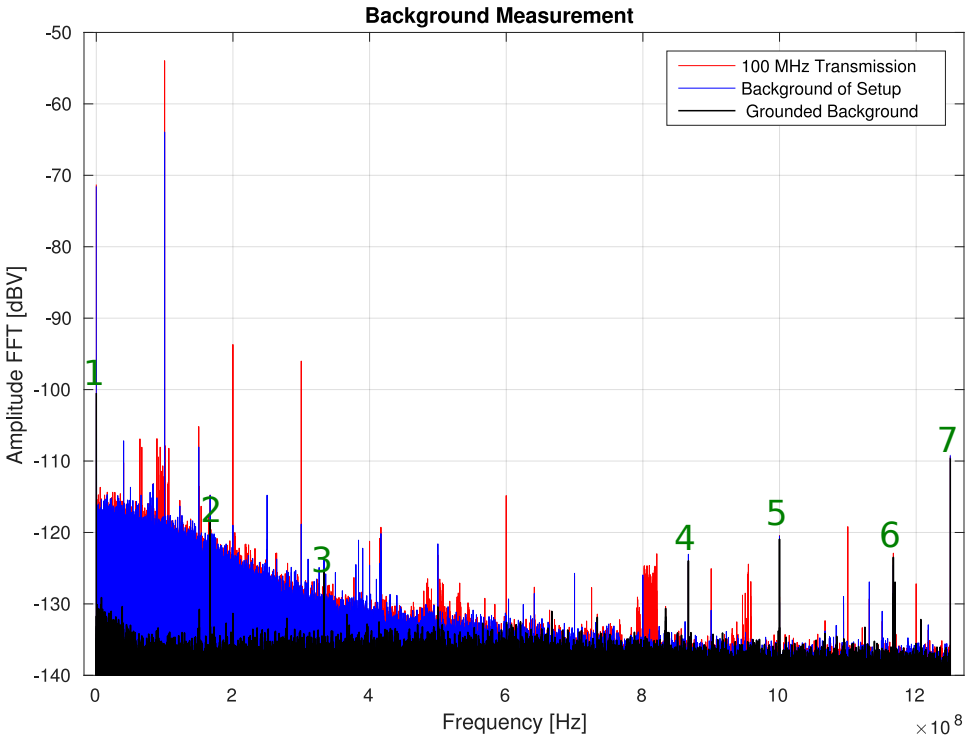

Figure 3.3: Comparison of Background Noise and Signal

Table 3.4: Peaks in FFT of the Grounded Spectrum

Peak Number	2	3	4	5	6
Frequency [MHz]	166,593	333,320	866,615	999,948	1,166,612
Amplitude [dBV]	-118.6	-125.3	-124.0	-120.9	-123.5

The spectrum of the BSM exhibits even more peaks and more importantly all lower frequencies till approximately 600 MHz show a larger amplitude as higher frequencies above 600 MHz. It also exhibits a peak at 100 MHz.

In the spectrum of the measurement with a 100 MHz signal the peak at 100 MHz is distinguishable from its surrounding frequencies. The spectrum also exhibits the higher harmonics of the 100 MHz signal and peaks at frequencies where no peaks were detected in the noise measurements but with much lower amplitudes than the peak at 100 MHz and its harmonics.

Discussion

The five peaks listed in table 3.4 are probably caused by internal electronics of the oscilloscope because the combination of covering channel 1 with a 50 Ω cab and internally grounding it should prevent the oscilloscope from measuring any external signals. The increased amplitudes for frequencies below 100 MHz are due to the 100 MHz bandwidth of the oscilloscope. The bandwidth acts as a low-pass filter, attenuating all frequencies higher than 100 MHz to less than 70.7 % of their true amplitude Tektronix (2012*a*). Thus, an oscilloscope with a bandwidth of at least 200 MHz would be better suited to cover the full range of the expected RF-emission by the NNP. This also means that for all peaks at frequencies above 100 MHz the oscilloscope does not measure the correct amplitude due to the attenuating effect of the bandwidth. The bandwidth of an oscilloscope is determined by its front-input amplifier, i.e. the amplifier amplifies all signal till the frequency of the bandwidth.

In case of the BSM the spectrum can be divided into three section. In section one from 0 MHz until 100 MHz the signal is amplified by the front-input amplifier and consequently does not show

attenuating effects. Section two from $100MHz$ until $600MHz$ shows the noise contribution due to the external signal with the attenuating effect of the bandwidth. Section three for frequencies above $600MHz$ only exhibits the white noise components of the signal, which are also present without external input. The reason why the BSM also exhibits a peak at 100 MHz is probably due to the fact, that even though the output of the function generator was turned off it still influenced the measurement.

The distinct peak at 100 MHz for the 100 MHz transmission measurement shows that over short distances (12 cm) a transmission of a signal between the antennas is possible. Besides the 100 MHz and its higher harmonics the spectrum also exhibits a distinct group of peaks in the region of 791 MHz until 820.5 MHz. Due to the bandwidth of the oscilloscope the amplitudes of these peaks is underestimated in figure 3.3 and would be considerably higher for an oscilloscope with a lager bandwidth. According to the Office of Communications in the United Kingdom these peaks fall into the frequency range of the 4 G mobile broadband services, which in use since 2013 (Ofcom 2012). Hence, the antenna probably detected strong signals from this broadband. Why the peaks are not seen in the BSM spectrum is not yet clear.

As all spectra with and without an incoming signal exhibit different amplitudes for different peaks, it is important to conduct noise measurements before every series of measurements on the NNP to identify peaks that are caused by background noise.

Antenna Measurements for Different Distances and Frequencies

To determine the best frequency for transmission measurements on the Gabor lens the antenna test setup shown in figure 2.15 was used and the frequency and the distance between them were altered. In Figure 3.4 the amplitude measured for a pre-set frequency is plotted against the distance between the antennas. The distance between the antennas was measured with a ruler hence the error in x direction is ± 0.1 cm. The error in amplitude was assumed to be ± 3 dBV for the y direction. The difference at 63 cm between 100 MHz and 130 MHz is 7 dBV and between 100 MHz and 70 MHz it is 14 dBV.

Discussion

The results of the transmission measurements imply that for transmission measurements on the lens a 100 MHz signal should produce the best results and increasing the frequency should produce better results than reducing it. Figure 3.4 also shows the anticipated overall decrease in amplitude over distance but not as monotone as expected for free space propagation (McCune 2010, p. 249). That the amplitude did not decrease as monotone over distance as expected could be explained by different reflections of the signal for different measurements, which can alter the polarization of the signal and consequently reduce or increase the signal strength reaching the receiving antenna. Additionally, the different reflected and not reflected signals can destructively or constructively interfere with each other influencing the amplitude received at antenna 1.

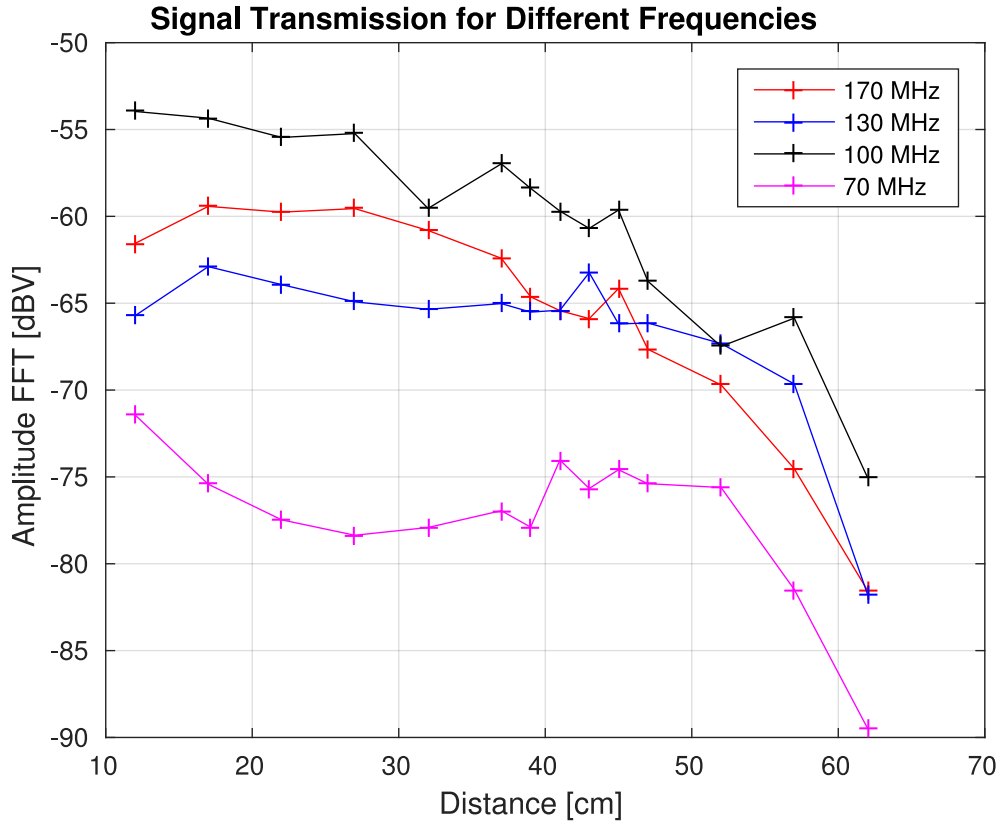

Figure 3.4: Comparison of Amplitudes for Different Distances and Frequencies
For clarity of graph error bars were omitted and measure ±0.1 cm in x direction and ±3 dBV in y direction.

Antenna Measurements for Orthogonal Orientation

As explained in chapter 2.5.1, the transmission of a signal between two antennas depends on matching the polarization of the antennas. In theory if two linear polarized antennas are installed at a right angle the transmitted signal should be zero because the signal is reduced by a factor of cosine of the angle between the antennas. If A_1 is the amplitude emitted from the sending antenna, A_2 the amplitude measured at the receiving antenna and 90° the angle between the antennas equation 3.1 expresses their relation:

$$A_2 = \cos\left(\frac{\pi}{2}\right) \cdot A_1 = 0. \tag{3.1}$$

Figure 3.5 shows the amplitudes for a 100 MHz transmission with parallel and orthogonal mounted antennas for different distances using the antenna test setup shown in figure 2.15. The mean difference ΔA_{PO} between the amplitudes of the parallel and orthogonal mounted antennas is (5.82±1.92) dBV.

Discussion

According to theory it would be expected that no signal is detected for the orthogonal mounted antennas. But even though the amplitude is (5.82±1.92) dBV smaller in this case than for the parallel setup the signal does not vanish. Possible reasons for the signal not to vanish are that the antennas were mounted by eyesight, therefore the angle is only approximately 90 degree, the antennas are not completely straight influencing the angle as well. Additionally, reflections can alter the polarization of the transmitted signal. Hence, the polarization of the emitted signal can alter from the polarization of the received signal, which is the sum over all transmitted signals, i.e. the directly transmitted ones as well as the reflected ones.

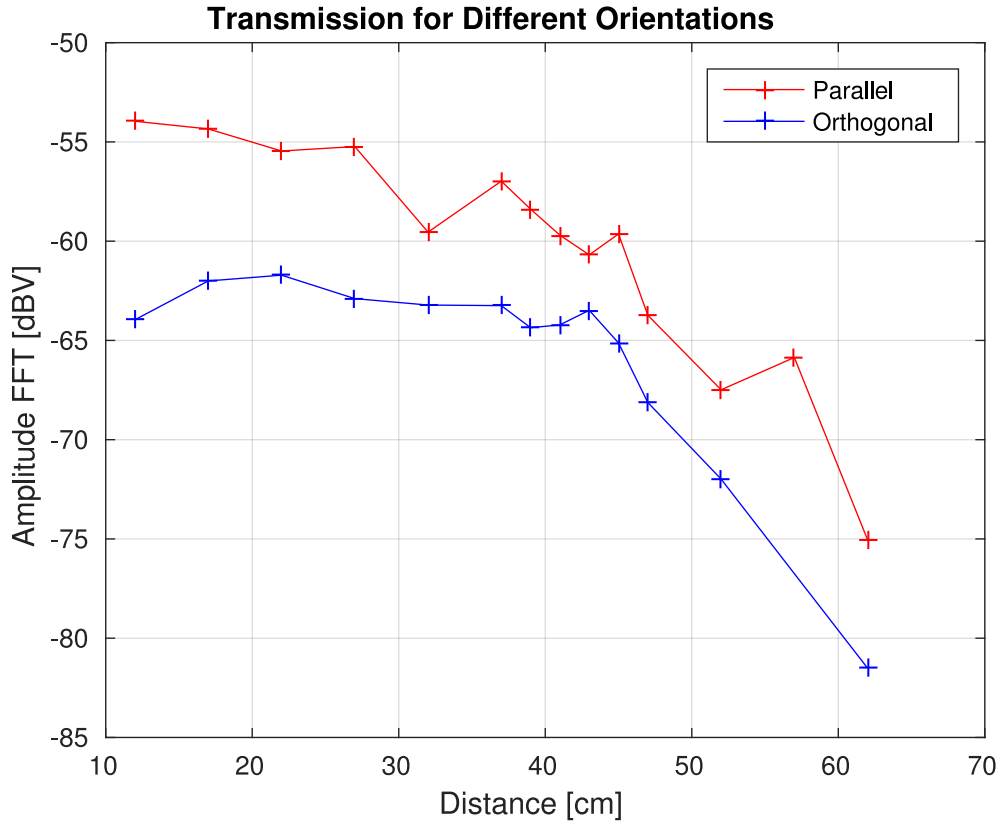

Figure 3.5: Comparison of Parallel and Orthogonal Mounted Antennas
For clarity of graph error bars were omitted and measure ±0.1 cm in x direction and ±3 dBV in y direction.

Unexpected Peak

Three measurements from the 13 March 2018 showed an unexpected peak at 14.8 MHz. This peak has not been seen during any other measurements. The frequency of 14.8 MHz falls into the range of shortwave radio transmission. Figure 3.6 shows the detected peak at 14.8 MHz, circled in red, during a 170 MHz transmission measurement. It has an amplitude of -82.54 dBV, which is only 20.13 dBV less than the amplitude of the 170 MHz peak. The spectrum additionally exhibits the group of peaks in the frequency range from 791 MHz until 820.5 MHz, which were also detected in chapter 3.3.1.

Discussion

As the unexpected peak lies in the range of shortwave radio transmission it is probable that the receiving antenna detected a signal from the two large antennas, which are mounted on the rooftop of the building opposite the accelerator lab. The detection of such a strong external signal in the range of the expected RF-signal from the NNP underlines the importance of a good shielding for experiments on the Gabor lens.

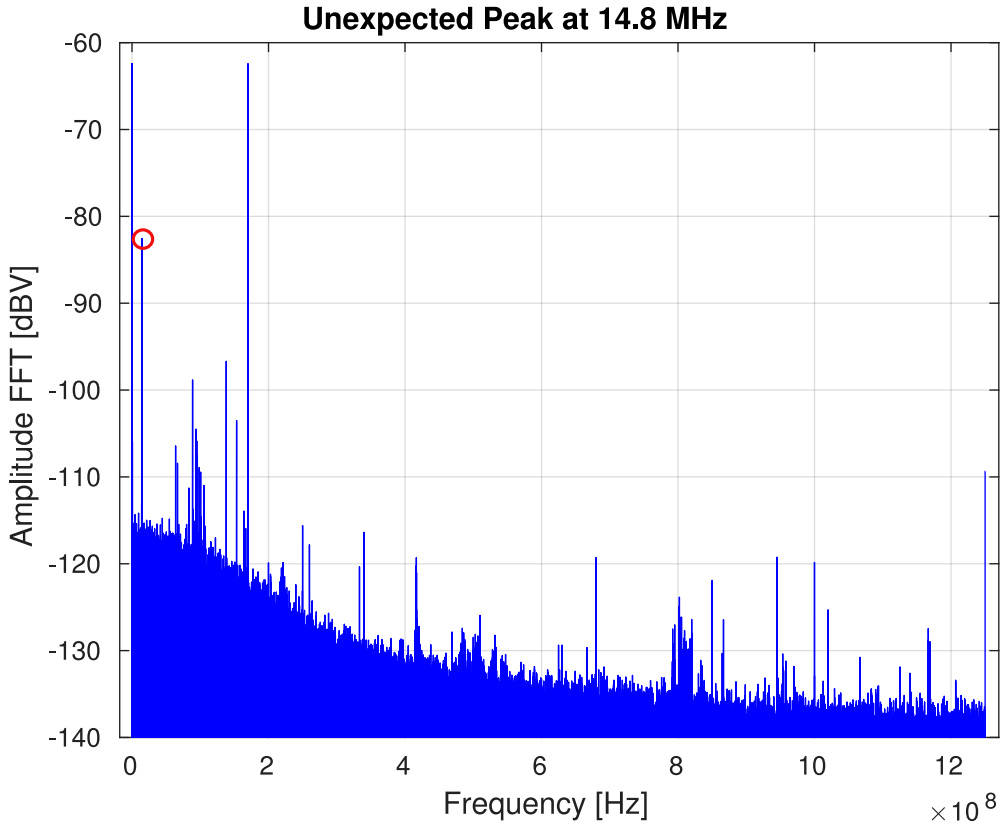

Figure 3.6: Unexpected Peak 14.8 MHz

3.3.2 RF-Emission Measurements with Burning NNP at 10^{-6} mbar

In chapter 3.2.2 it was discussed that the pressure inside the Gabor lens could not be brought down to 10^{-7} mbar due to a vacuum leak. Hence, the lens was operated at 2.83×10^{-6} mbar for the test measurements on the NNP. In the setup proposed in chapter 2.5.4 antenna 2 in the horizontal position was replaced by a CA.96 antenna to compare the performance of both antenna types. By mounting the CA.96 antenna in horizontal direction it matches the vertical polarization of the self build antenna, which is mounted in vertical orientation. Table 3.5 summarizes the settings of the oscilloscope. The FFT was computed in MATLAB using the Hanning window. Changing the coil

Table 3.5: Oscilloscope Settings for Emission Measurement

Parameter	Value
Acquisition Mode	Sample
Horizontal Scale	0.002 s
Sample Interval	2×10^{-9}
Record Length	10^6 Points
Vertical Scale	0.01 V

current and the high voltage supply for the electrode system generates different states of NNP. Table 3.6 summarizes the settings, which were used to generate the different states. In case of the stable NNP a precise value of the pressure is missing because only an slight increase in pressure was recorded in the record of the experiment. To support the hypothesis, that the rotation of an electron bulk inside the Gabor lens caused the conversion of an incoming pencil proton beam into a ring shaped pattern on the scintillator, it would be expected to detect a rotation frequency in the amplitude spectrum of the stable NNP (SP), which is not present in the reference measurement (RM) without NNP. For this purpose the amplitude spectra of the SP were compared to the spectra of the reference RM and to the unstable NNP (UP) states for each antenna. Figure 3.7 shows the spectra measured for the RM.

Table 3.6: Parameters for the Generation of Different NNP States

	Solenoid Supply		High Voltage Supply		
Name	Voltage [V]	I [A]	Voltage [kV]	I [mA]	Pressure [mbar]
Reference	0	0	0	0	2.83×10^{-6}
Stable NNP	7.0	23.6	25.1	0.02	$< 10^{-5}$
Unstable NNP 1	11.4	38.2	10.7	1.06*	1.89×10^{-5}
Unstable NNP 2	14.2	46.9	7.6	1.06*	1.90×10^{-5}
Unstable NNP 3	14.4	46.9	3.6	5*	4.72×10^{-5}

*: in this cases the current of the HV supply was limited.

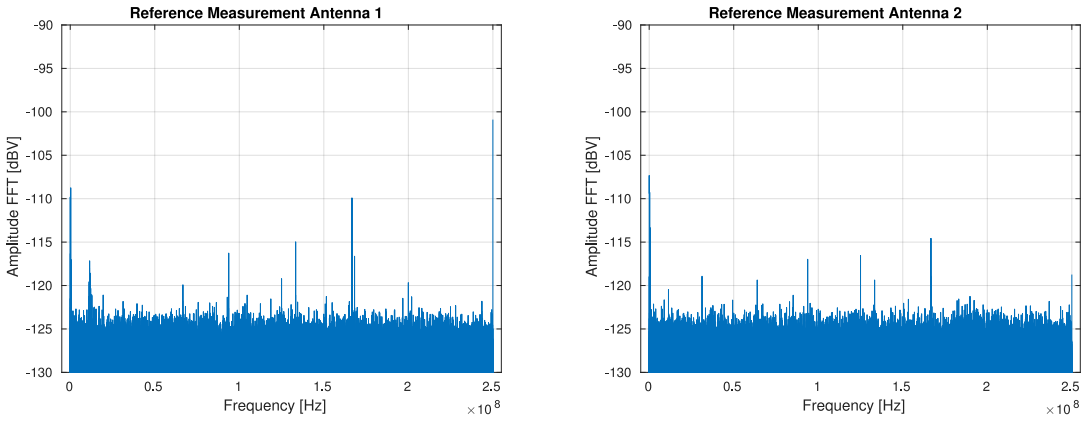

(a) Amplitude Spectrum of Antenna 1

(b) Amplitude Spectrum of Antenna 2

Figure 3.7: Spectra of the Reference Measurement

For the individual measurements all frequencies between 1 MHz and 200 MHz with an amplitude above -120 dBV are listed in the tables A.1 till A.3 for antenna 1 and in the table A.4 and A.5 for antenna 2, see appendix A. The frequencies, which were detected in the spectra of the SP and not in the spectra of the RM are listed in table 3.7. For the RM antenna 1 detected twenty one peaks, which meet the requirements, whereas antenna 2 only detected nine peaks. But these nine peaks were at identical frequencies as the nine peaks measured by antenna 1. In the case of antenna 1 the spectrum of the SP exhibits three additional peaks, which were not present in the spectrum of RM but also misses ten peaks, which were detected in the RM. In the case of antenna 2 the spectrum of the SP exhibits all but the one peak at 63.90 MHz, detected in the RM. It also detected two additional peaks but at different frequencies than antenna 1.

Table 3.7: Additional Peaks Detected in the SP

			Antenna 1		Antenna 2
f [MHz]	5.90	165.08	166.67	82.04	200.00
RM A [dBV]	/	/	/	/	/
SP A [dBV]	-119.09	-117.46	-119.35	-119.89	-117.92
UP 1 A [dBV]	/	-119.63	-118.60	/	/
UP 2 A [dBV]	/	-109.55	119.99	/	-117.59
UP 3 A [dBV]	/	/	-118.46	/	-119.18

Figure 3.9 till figure 3.11 show the spectra of the measurements on UP states. UP 2 was generated with maximum solenoid current and represents the state of maximal radial confinement. UP 3 was generated with maximum current for the electrode system. For antenna 1 all but the last two frequencies detected in the RM were also detected in all of the measurements on UP states. Moreover, the third peak additionally detected in the spectrum of the SP was also detected in every of these measurement. The second additional peak detected in the spectrum of the SP was also detected in the spectrum of the UP 1. The first peak at 0.59 MHz was not detected in any other measurement. For antenna 2 all but the peaks at 31.25 MHz and 63.90 MHz detected in the

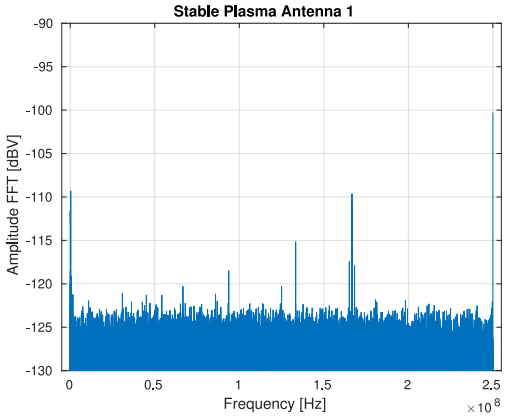

(a) Amplitude Spectrum of Antenna 1

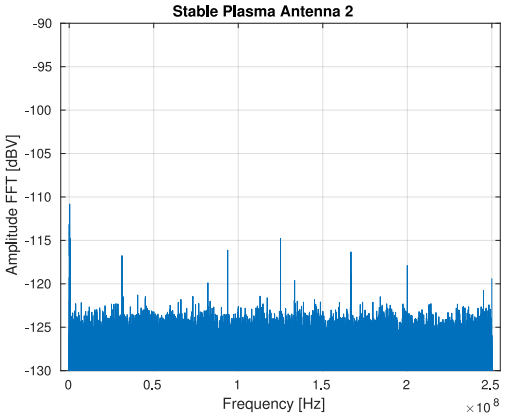

(b) Amplitude Spectrum of Antenna 2

Figure 3.8: Spectra of the Stable NNP State

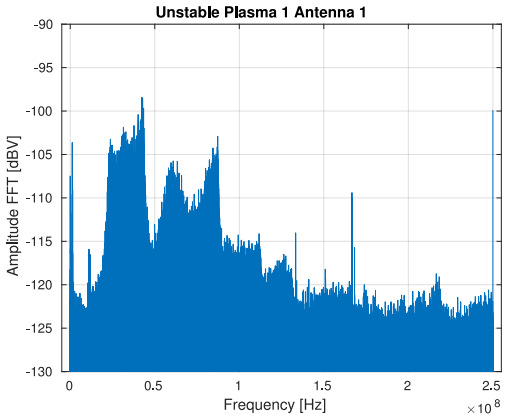

(a) Amplitude Spectrum of Antenna 1

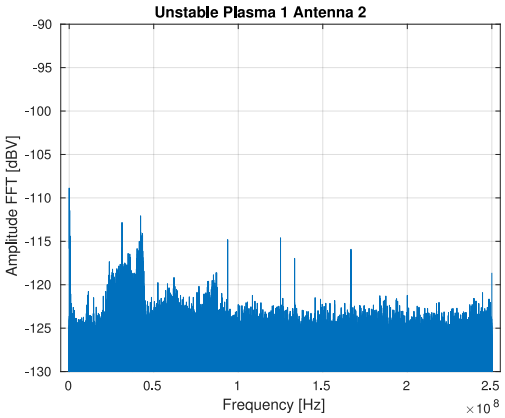

(b) Amplitude Spectrum of Antenna 2

Figure 3.9: Spectra of the Unstable NNP State 1

RM were also detected in all later measurements but these two peaks were only missing in one or respectively two measurements. Concerning the two additional peaks detected in the spectrum of the SP, the first one at 82.04 MHz was not detected in any other measurement, whereas the second peak at 200 MHz was detected in other measurements with antenna 2 as well and also in the spectrum of antenna 1 for the RM.

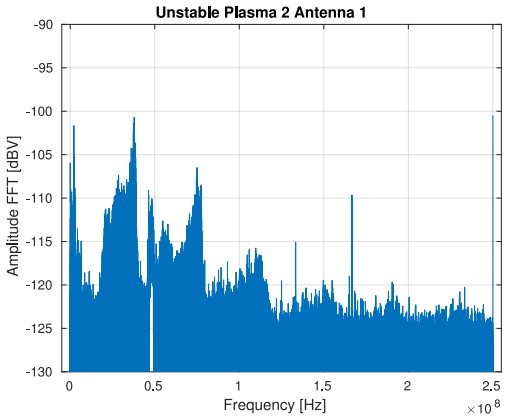

(a) Amplitude Spectrum of Antenna 1

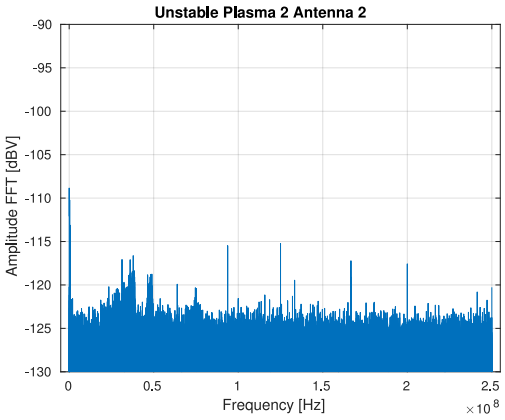

(b) Amplitude Spectrum of Antenna 2

Figure 3.10: Spectra of the Unstable NNP State 2

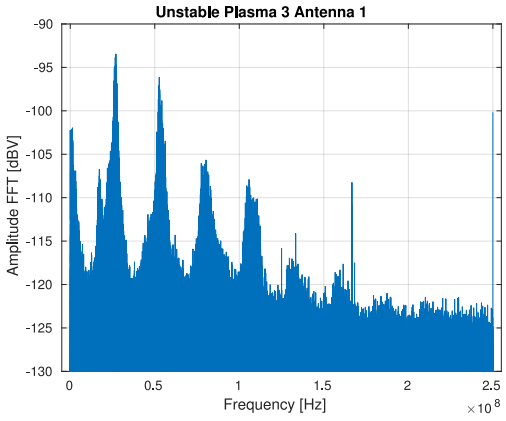

(a) Amplitude Spectrum of Antenna 1

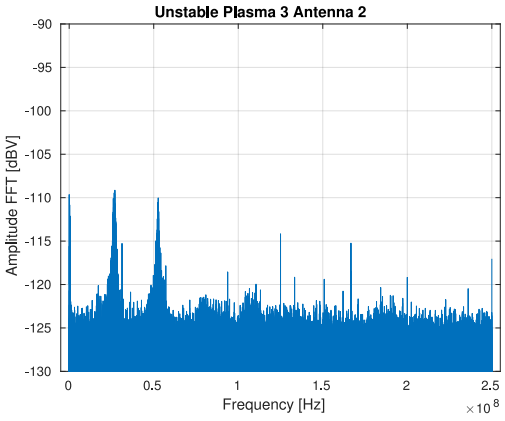

(b) Amplitude Spectrum of Antenna 2

Figure 3.11: Spectra of the Unstable NNP State 3

Discussion

None of the spectra acquired during the RF-emission measurements show the attenuating effect of the oscilloscope's 100 MHz bandwidth, which was detected in chapter 3.3.1 and chapter 3.3.1. On account of the settings of the oscilloscope this effect has not been explained yet and further experiments would be necessary to identify the cause of the missing attenuation.

For the following reasons the results do not indicate that any of the peaks, which were additionally detected in the spectra of the SP are related to a rotation frequency of an rotating electron bulk inside the Gabor lens. Firstly, the additional peaks were different for both antennas and their amplitudes were between 8.65 dBV and 10.62 dBV lower than the amplitude of the highest peak in the RM. This makes it more plausible that the peaks are related to external RF-sources. Secondly, all but two peaks were also detected in the spectra of the UP states. This implies that they are not special to the case of the SP and consequently are probably caused by another source than the rotation of an electron bulk in the SP. The spectra of the UP states indicate that both antennas are capable of detecting RF-emissions from the NNP. The much higher amplitudes detected in the spectra of the UP states can be explained by the at least 50 times greater currents provided by the HV supply. The spectra also show that the two antennas detect signals at the same frequencies, which supports the argument that the peaks detected for the SP are not related a to RF-emission from the NNP because they are at different frequencies. The considerable difference in amplitude for the two antennas could be due to the fact, that the CA.96 antenna is specifically designed for a centre frequency of 169 MHz and consequently has a small bandwidth of 8 MHz whereas the self-build antennas seem to work best at frequencies around 100 MHz and probably have a larger bandwidth, because they are not especially designed for a certain frequency, see chapter 3.3.1. The fact that most of the peaks detected by the antennas during the RM were also detected in measurements on stable and unstable NNP states indicates a stable background in the range of 1 MHz to 200 MHz. The fact that no peak was detected in the spectra of the SP does not mean that the NNP did not emit a RF-signal. Possible reasons why a RF-signal emitted by an rotating electron bulk in the SP might not have been detected are:

1. The Trajectory of the electron bulk is a helix
2. Signal strength is considerably smaller compared to UP states
3. Attenuation of signal in circular waveguide
4. Attenuation of signal by vacuum window and plastic cab of shielding
5. Shielding does not suppress background noise well enough to detect weaker signal from lens.

3.3.3 Transmission Measurement with the Gabor Lens

As preparation for transmission measurements on the burning NNP test measurements without NNP were conducted for different frequencies between 20 MHz and 200 MHz. For this purpose the setup proposed in chapter 2.5.4 was used. The two self-build antennas were used in crossed configuration because the self-build antenna detected more signal than the CA.96 antenna during the previous RF-emission measurements. Antenna 1 was mounted in the vertical orientation and antenna 2 was mounted in horizontal orientation. The settings of the oscilloscope are summarized in table 3.8. The FFT was computed in MATLAB using the Hanning window. The acquisition

Table 3.8: Oscilloscope Settings for Transmission Measurements

Parameter	Value
Acquisition Mode	Average 8×
Horizontal Scale	2×10^{-8} s
Sample Interval	4×10^{-10}
Record Length	10^6 Points
Vertical Scale	0.001 V

mode was changed to 8× averaging to increase the stability and reproducibility of the amplitude spectra. The settings for the function generator are summarized in table 3.9. The spectra for 20 MHz, 100 MHz and 196 MHz are shown in Figure 3.12 till 3.15. The spectra for 50 MHz and

Table 3.9: Function Generator Settings for Transmission Measurements

Parameter	Value
Waveform	Sine
Amplitude	5.00 V_{pp}
Phase	0°
Offset	0.00 mV

200 MHZ can be found in appendix B. Table 3.10 summarizes the amplitudes for Antenna 1 for different frequencies. It additionally gives the amplitudes of the next two highest peaks found in the spectra. Similarly, table 3.11 summarizes the results for Antenna 2.

Table 3.10: Results for Antenna 1 of the Transmission Measurement

Transmission Peak		Peak Two		Peak Three	
f [MHz]	A [dBV]	f [MHz]	A [dBV]	f [MHz]	A [dBV]
20	/	83.39	-131.74	118.50	-132.64
50	/	83.34	-130.75	150.00	-131.00
100	-121.25	83.33	-131.79	166.67	-133.41
100	-132.18	83.30	-132.62	83.27	-133.25
105	-115.61	83.65	-131.17	83.39	-131.83
169	-105.19	83.34	-131.26	83.67	-131.66
200	-101.99	83.39	-132.88	83.61	-133.06

Table 3.11: Results for Antenna 2 of the Transmission Measurement

Transmission Peak		Peak Two		Peak Three	
f [MHz]	A [dBV]	f [MHz]	A [dBV]	f [MHz]	A [dBV]
20	-128.51	75.43	-126.91	90.22	-126.91
50	-123.92	66.67	-125.09	122.36	-134.84
100	-106.38	153.32	-124.23	153.33	-131.40
100	-116.72	66.7	-134.50	83.11	-135.98
105	-101.49	153.32	-124.25	153.33	-125.97
169	-110.12	79.87	-132.58	66.67	-133.09
200	-102.36	66.67	-125.68	33.12	-132.44

The 20 MHz and the 50 MHz signal were only detected by antenna 2 but all other signals were detected by both antennas. Additionally, antenna 1 detected at least one peak at 83.35 ± 0.05 MHz for all transmission measurements. The repetition of the 100 MHz transmission measurement shown in figure 3.14 showed that the amplitude for the 100 MHz peak varies for different measurements with identical parameters. In case of antenna 1 the repetition measurement showed a 10.93 dBV lower peak and for antenna 2 a 10.34 dBV lower one.

Discussion

The transmission measurements demonstrated that it is possible to transmit a singal through the Gabor Lens without NNP, which was generated with an amplitude of 5.00 V_{pp} by the function generator. Due to the different orientations in which the self-build antennas were mounted and the fact that thy are not identical their spectra for the individual measurements differ. The difference in construction result in different transfer characteristics for the twa antennas. The difference in amplitude for the two 100 MHz transmissions of 10 dBV in case of antenna 1 and 10.34 dBV in case of antenna 2 underlines the uncertainty in the determination of the amplitude for different measurements conducted with the same parameters. This effect has been seen during all of the background and transmission measurements and changing the acquisition mode to 8 times averaging did not eliminate the effect. To increase the stability of the amplitude determination in future experiments it might be reasonable to conduct at least seven consecutive measurements with identical parameter and to average the individual amplitudes. Thus, obtaining a meaningful mean amplitude and standard deviation for a set of parameters. Following the argument form

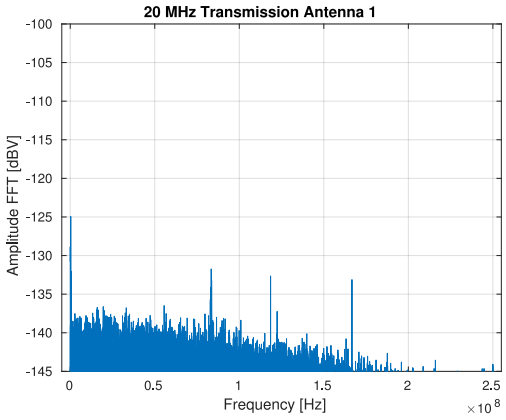

(a) Amplitude Spectrum of Antenna 1

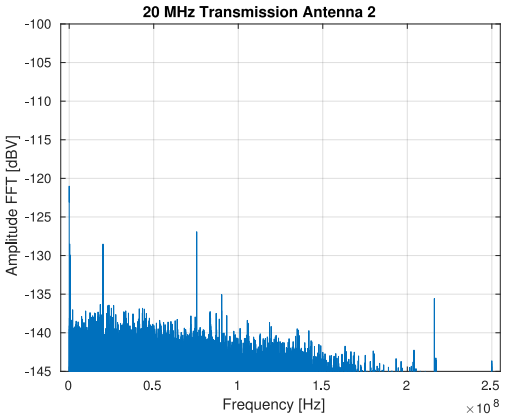

(b) Amplitude Spectrum of Antenna 2

Figure 3.12: Transmission Measurement at 20 MHz

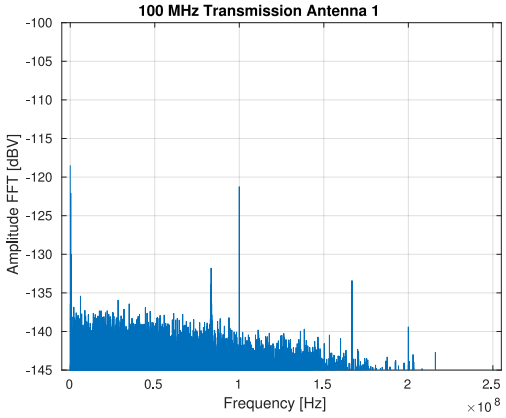

(a) Amplitude Spectrum of Antenna 1

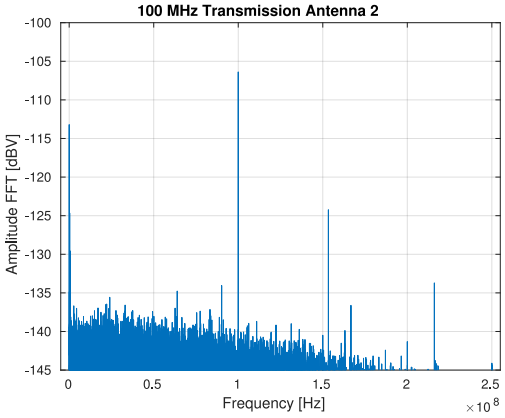

(b) Amplitude Spectrum of Antenna 2

Figure 3.13: Transmission Measurement at 100 MHz

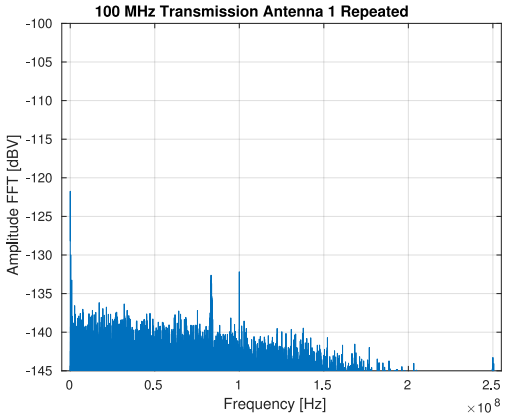

(a) Amplitude Spectrum of Antenna 1

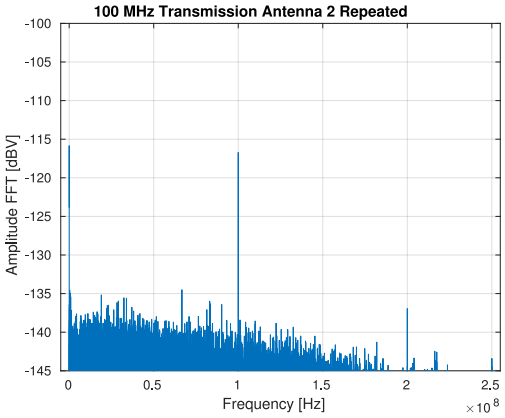

(b) Amplitude Spectrum of Antenna 2

Figure 3.14: Repetition of Transmission Measurement at 100 MHz

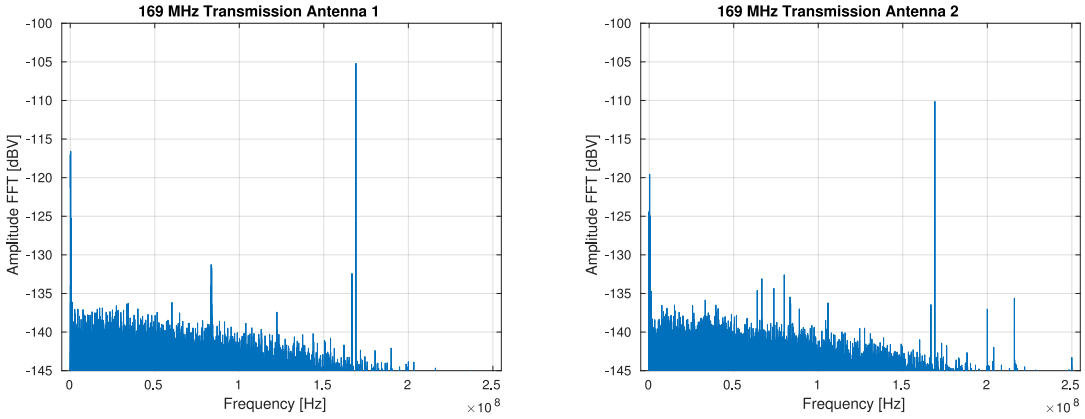

(a) Amplitude Spectrum of Antenna 1

(b) Amplitude Spectrum of Antenna 2

Figure 3.15: Transmission Measurement at 169 MHz

chapter 3.3.1 the difference in amplitude might be caused by the difference in reflections and consequently interference pattern of the transmitted signal for each measurement. The uncertainty in the determination of amplitudes of individual signals makes the detection of low-amplitude signals difficult.

Chapter 4

Summary and Outlook

In chapter 3.2 it was established that the Gabor lens prototype has a vacuum leak and that a dedicated helium detector is required for its precise localisation.

Chapter 3.3.1 proved the capability of the two self-build antennas to transmit a RF-signal over distances up to 60 cm. Moreover, the influence of background noise, external RF-sources and the bandwidth of the oscilloscope were studied, underlining the importance of a good shielding and frequent reference measurements for later experiments on the NNP confined within it Gabor lens.

To identify the cause of the conversion of a proton pencil beam into rings by the Gabor lens prototype two experiments were designed and tested. In Chapter 3.3.2 the RF-emission measurements showed that both antenna types (self-build and taoglas CA.69) are capable of detecting RF-emissions by unstable plasma states. In the case of the SP, which is best suitable for ion beam focussing, no signal which would indicate a RF-emission of an rotating electron bulk, was detected. Five possible reasons were identified, why a signal emitted by the SP might not have been detected. A first step to improve the setup would be to improve the shielding of the antennas in order to make the system more sensitive to low amplitude signals. In a second step a new set of antennas could be build or purchased, which can be installed inside the waveguide. This would reduce the attenuating effects of the waveguide and the vacuum window, allowing the detection of weaker signals emitted by the SP state. To install these antennas in the vacuum system of the Gabor lens the antennas would need a vacuum feedthrough and have to be manufactured out of vacuum compatible materials. Due to the fact that in chapter 3.3.3 the $5\,V_{pp}$ signals used for the transmission measurements were clearly detected the RF-signal emitted by the SP state would have to be even weaker. This in improbable due to the current of 0.02 mA provided by the HV-supply for its ignition. Hence, all the improvements to detect weaker signals might prove to be in vain. This would support the idea of an electron bulk following the path of a helix. A helical trajectory could explain why the proton pencil beam was converted into rings but no rotation frequency was detected for the SP state.

The transmission measurements showed that a signal generated by the function generator and sent by a CA.96 antenna can be transmitted through the Gabor lens and detected by the crossed configuration of self-build antennas. This setup can be used to transmit a signal through the SP state and measure its influence on the transmission, allowing conclusions on its density. All these improvements would help to measure a potential RF-emission of the SP state and investigate its density.

In order to further investigate the feasibility of the Gabor lens prototype for in vitro experiments with laser-accelerate ions the vacuum leak has to be localized and closed and the reason for the proton beam conversion has to be further investigated and resolved. Afterwards the results from chapter 3.1 on ion beam energies and magnetic rigidities could be used for the design of a suitable beamline and radiobiological end-station. The studies showed that the application of ions heavier than protons in in vitro experiments considerably increases the requirements on the laser system due to the higher energies heavier ions need to pass through matter. It was also shown that bending heavier ion beams increases the requirements for the dipole magnet due to their increased resistance to deflection.

Appendix A

First Appendix

Table A.1: Results Antenna 1

f [MHz] A [dBV] of	0.30	0.5900	0.5905	11.16	11.29	11.411	11.47
Reference	-108.75	/	-117.02	-119.56	-119.81	-118.00	-117.15
Stable Plasma	-109.27	-119.09	/	/	/	/	/
Unstable Plasma 1	-109.62	/	-118.10	/	/	-117.72	-119.63
Unstable Plasma 2	-118.21	/	-115.77	/	/	/	/
Unstable Plasma 3	-107.24	/	-109.69	/	/	/	/

Table A.2: Results Antenna 1 Part 2

11.66	11.79	66.65	93.75	125.00	133.34	165.08	166.63
-119.00	-118.57	-119.91	-116.26	-119.21	-114.97	/	-109.95
/	/	/	-118.52	/	-115.17	-117.46	-111.18
/	-116.53	/	-117.79	-119.85	-114.05	-119.63	-109.41
/	/	/	-119.67	-119.53	-115.08	-109.55	
/	/	-119.02	-118.53	-115.88	-114.13	/	108.25

Table A.3: Results Antenna 1 Part 3

166.64	166.65	166.67	166.68	166.70	168.18	200.00
-115.08	-109.94	-119.32	-119.89	/	-116.63	-119.67
-116.43	-109.64	-116.35	-119.74	-119.35	-117.92	/
-115.35	-110.00	-118.60	-119.32	-118.60	-115.71	/
-114.69	-109.68	-116.85	-119.41	-119.99	/	/
-113.46	-110.80	-116.86	-118.65	-118.46	/	/

Table A.4: Results Antenna 2

f [MHz] A [dBV] of	0.30	0.5905	31.25	63.90	82.04	93.75	125.00
Reference	-109.27	-113.34	-118.93	-119.38	/	-116.98	-116.56
Stable Plasma	-110.81	-114.79	-116.77	/	-119.89	-116.11	-114.81
Unstable Plasma 1	-111.46	-114.40	-112.83	/	/	-114.80	-114.62
Unstable Plasma 2	-110.21	-113.12	-117.07	-119.91	/	-115.49	-115.22
Unstable Plasma 3	-110.83	-112.12	-115.27	/	/	-118.57	-114.18

Table A.5: Results Antenna 2 Part 2

133.34	166.67	166.68	200.00
-118.00	-117.15	-119.00	-118.57
-119.60	-116.34	-118.82	-117.92
-116.96	-116.16	-115.92	/
-119.45	-117.23	-119.08	-117.59
-119.16	-115.23	-118.45	-119.18

Appendix B

Second Appendix

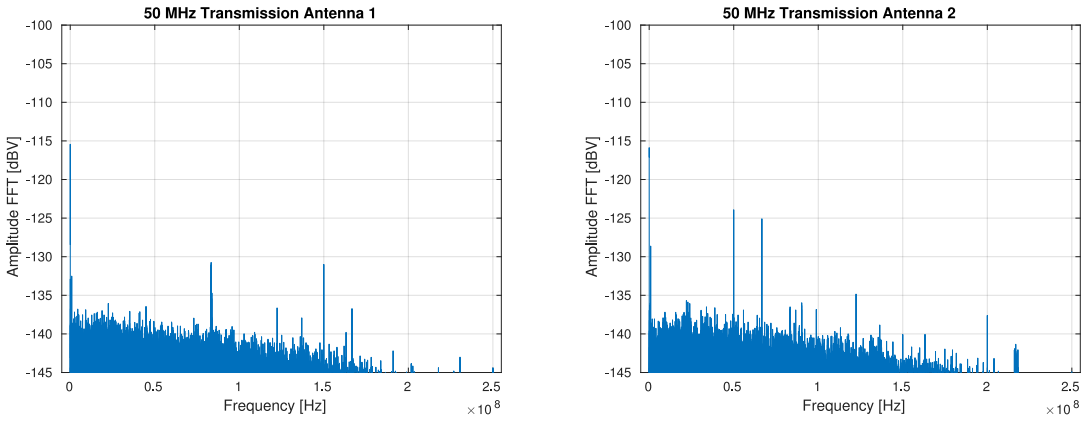

(a) Amplitude Spectrum of Antenna 1

(b) Amplitude Spectrum of Antenna 2

Figure B.1: Transmission Measurement at 50 MHz

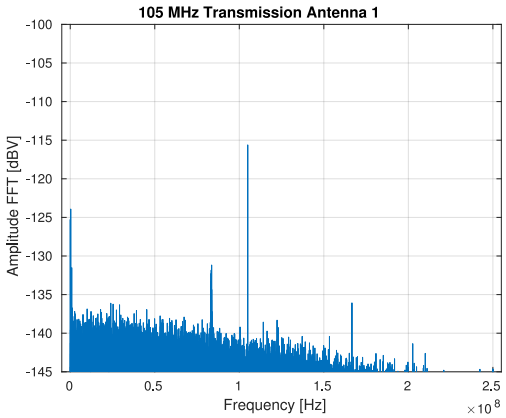

(a) Amplitude Spectrum of Antenna 1

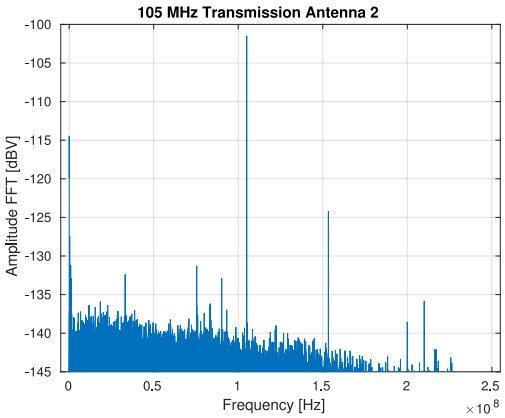

(b) Spectrum of Antenna 2

Figure B.2: Transmission Measurement at 105 MHz

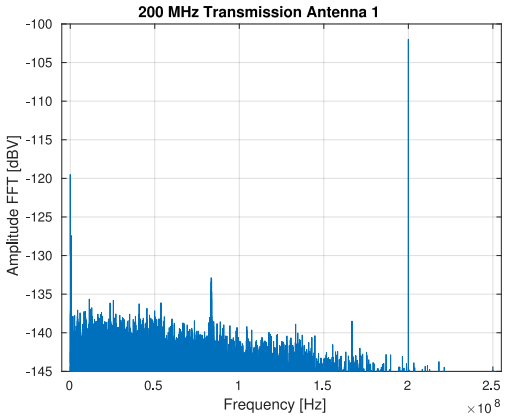

(a) Amplitude Spectrum of Antenna 1

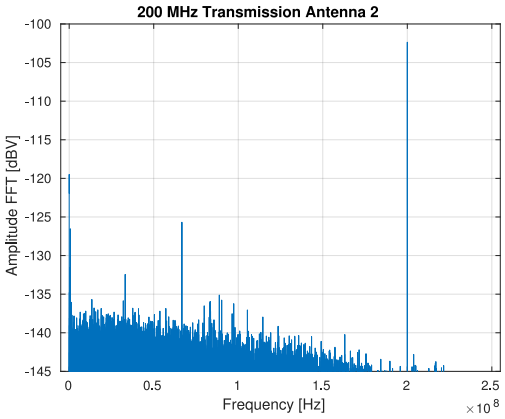

(b) Amplitude Spectrum of Antenna 2

Figure B.3: Transmission Measurement at 200 MHz

Bibliography

Aragon-Zavala, A. (2008), *Antennas and propagation for wireless communication systems*, Chichester: John Wiley & Sons.

Baskar, R., Lee, K. A., Yeo, R. & Yeoh, K.-W. (2012), 'Cancer and radiation therapy: current advances and future directions', *International journal of medical sciences* **9**(3), 193.

Bray, F., Ferlay, J., Soerjomataram, I., Siegel, R. L., Torre, L. A. & Jemal, A. (2018), 'Global cancer statistics 2018: Globocan estimates of incidence and mortality worldwide for 36 cancers in 185 countries', *CA: A Cancer Journal for Clinicians* .

Bulanov, S. & Khoroshkov, V. (2002), 'Feasibility of using laser ion accelerators in proton therapy', *Plasma Physics Reports* **28**(5), 453–456.

Bulanov, S. V., Wilkens, J. J., Esirkepov, T. Z., Korn, G., Kraft, G., Kraft, S. D., Molls, M. & Khoroshkov, V. S. (2014), 'Laser ion acceleration for hadron therapy', *Physics-Uspekhi* **57**(12), 1149.

Chen, G., Castro, J. & Quivey, J. (1981), 'Heavy charged particle radiotherapy', *Annual review of biophysics and bioengineering* **10**(1), 499–529.

Chu, W., Ludewigt, B. & Renner, T. (1993), 'Instrumentation for treatment of cancer using proton and light-ion beams', *Review of Scientific Instruments* **64**(8), 2055–2122.

Davidson, R. C. (2001), *Physics of nonneutral plasmas*, London: World Scientific Publishing Company.

Debus, J., Haberer, T., Schulz-Ertner, D., Jäkel, O., Wenz, F., Enghardt, W., Schlegel, W., Kraft, G. & Wannenmacher, M. (2000), 'Carbon ion irradiation of skull base tumors at gsi. first clinical results and future perspectives', *Strahlentherapie und Onkologie: Organ der Deutschen Rontgengesellschaft* **176**(5), 211–216.

Durante, M. & Loeffler, J. S. (2010), 'Charged particles in radiation oncology', *Nature reviews Clinical oncology* **7**(1), 37.

Gabor, D. (1947), 'A space-charge lens for the focusing of ion beams', *Nature* **160**(4055), 89.

Haberer, T., Becher, W., Schardt, D. & Kraft, G. (1993), 'Magnetic scanning system for heavy ion therapy', *Nuclear Instruments and Methods in Physics Research Section A: Accelerators, Spectrometers, Detectors and Associated Equipment* **330**(1-2), 296–305.

Hughes, C. (2014), 'Gabor lenses for focusing and energy selection of laser-driven ion beams in radiobiological experiments'. Imperial College London.

Kraft, S., Richter, C., Zeil, K., Baumann, M., Beyreuther, E., Bock, S., Bussmann, M., Cowan, T., Dammene, Y., Enghardt, W. et al. (2010), 'Dose-dependent biological damage of tumour cells by laser-accelerated proton beams', *New Journal of Physics* **12**(8), 085003.

Learn.Genetics (2018), 'Cell size and scale'. Accessed: 2018-09-25.
URL: *https://learn.genetics.utah.edu/content/cells/scale/*

MathWorks (2018), 'Fast fourier transformation'. Accessed: 2018-09-25.
URL: *https://uk.mathworks.com/help/matlab/ref/fft.html*

McCune, E. (2010), *Practical digital wireless signals*, Cambridge: Cambridge University Press.

Meusel, O. (2006), Fokussierung und Transport von Ionenstrahlen mit Raumladungslinsen, PhD thesis, Goethe-Universität Frankfurt.

Ofcom (2012), '800 mhz & 2.6 ghz combined award'. Accessed: 2018-10-21.
URL: *https://www.ofcom.org.uk/spectrum/spectrum-management/spectrum-awards/awards-archive/800mhz-2.6ghz*

Pedroni, E., Bacher, R., Blattmann, H., Böhringer, T., Coray, A., Lomax, A., Lin, S., Munkel, G., Scheib, S., Schneider, U. et al. (1995), 'The 200-mev proton therapy project at the paul scherrer institute: Conceptual design and practical realization', *Medical physics* **22**(1), 37–53.

Posocco, P. A., Xia, Y., Pozimski, J. & Merchant, M. (2016), 'First test of the imperial college gabor (plasma) lens prototype at the surrey ion beam centre'.

Pozimski, J. (1990), Messungen an einer Gabor-Plasma-Linse, PhD thesis.

Pozimski, J. (2017), '06-ccap meeting march 2017'. Accessed: 2018-10-20.
URL: *https://www.google.com/search?q=06-CCAPmeeting+March2017JP+forHEP+2&ie=utf-8&oe=utf-8&client=firefox-b-ab*

Pozimski, J. & Aslaninejad, M. (2013), 'Gabor lenses for capture and energy selection of laser driven ion beams in cancer treatment', *Laser and Particle Beams* **31**(4), 723–733.

Pozimski, J., Aslaninejad, M. & Posocco, P. A. (2016), Advanced gabor lens lattice for laser driven hadron therapy and other applications, *in* 'Proceedings of IPAC2016, Busan, Korea', TUPMY023, pp. 1595–1597.

Pozimski, J., Aslaninejad, M., Posocco, P. et al. (2013), Advanced gabor lens lattice for medical applications, *in* 'Proceedings of IPAC2013, Shanghai, China', TUPEA062, pp. 1277–1279.

Pozimski, J. & Meusel, O. (2005), 'Space charge lenses for particle beams', *Review of scientific instruments* **76**(6), 063308.

PTCOG (2018), 'Particle therapy facilities in operation'. Accessed: 2018-10-20.
URL: *https://www.ptcog.ch/index.php/facilities-in-operation*

Reiser, M. (1989), Comparison of gabor lens, gas focusing, and electrostatic quadrupole focusing for low-energy ion beams, *in* 'Particle Accelerator Conference, 1989. Accelerator Science and Technology., Proceedings of the 1989 IEEE', IEEE, pp. 1744–1747.

Richter, C., Karsch, L., Dammene, Y., Kraft, S., Metzkes, J., Schramm, U., Schürer, M., Sobiella, M., Weber, A., Zeil, K. et al. (2011), 'A dosimetric system for quantitative cell irradiation experiments with laser-accelerated protons', *Physics in Medicine & Biology* **56**(6), 1529.

Schardt, D., Elsässer, T. & Schulz-Ertner, D. (2010), 'Heavy-ion tumor therapy: Physical and radiobiological benefits', *Reviews of modern physics* **82**(1), 383.

Schulte, K. (2013), Studies on the focusing performance of a Gabor lens depending on nonneutral plasma properties, PhD thesis, Goethe-Universität Frankfurt.

Schwoerer, H., Pfotenhauer, S., Jäckel, O., Amthor, K.-U., Liesfeld, B., Ziegler, W., Sauerbrey, R., Ledingham, K. & Esirkepov, T. (2006), 'Laser-plasma acceleration of quasi-monoenergetic protons from microstructured targets', *Nature* **439**(7075), 445.

SIGMA (2010), 'Product information'. Accessed: 2018-09-25.
URL: *https://www.sigmaaldrich.com/content/dam/sigma-aldrich/docs/Sigma/Product_Information_Sheet/1/p7793pis.pdf*

Tektronix (2012*a*), '12 things to consider when choosing an oscilloscope'. Accessed: 2018-10-13.
URL: *https://www.mouser.com/pdfdocs/Tektronix12_things_to_consider1.pdf*

Tektronix (2012*b*), 'Mso3000 and dpo3000 series digital phosphor oscilloscopes user manual'. Accessed: 2018-10-21.
URL: *https://www.tek.com/bench-oscilloscopes/mso3000-dpo3000-manual/mso3000-and-dpo3000-series*

Tobias, C. A. & Todd, P. W. (1967), Heavy charged particles in cancer therapy., Technical report, Univ. of California, Berkeley.

Wilson, R. R. (1946), 'Radiological use of fast protons', *Radiology* **47**(5), 487–491.

Ziegler, J. F., Ziegler, M. D. & Biersack, J. P. (2008), *SRIM: the stopping and range of ions in matter*, Morrisville: Lulu Press Co.

Erklärung

Ich versichere, dass ich die Arbeit ohne fremde Hilfe und ohne Benutzung anderer als der angegebenen Quellen angefertigt habe und dass die Arbeit in gleicher oder ähnlicher Form noch keiner anderen Prüfungsbehörde vorgelegen hat und von dieser als Teil einer Prüfungsleistung angenommen wurde. Alle Ausführungen, die wörtlich oder sinngemäß übernommen wurden, sind als solche gekennzeichnet.

Erlangen, den 23. Oktober 2018

MORITZ SEBALD